Functional properties of citric acid capped TiO$_2$ nanoparticles by hydrothermal growth and dye-sensitized solar cell performance

J. Archana[1, 2], M. Navaneethan[2], and Y. Hayakawa[1, 2*]

1 Graduate School of Science and Technology, Shizuoka University
2 Research Institute of Electronics, Shizuoka University
3-5-1 Johoku, Naka-Ku, Hamamatsu, Shizuoka 432-8011, Japan.

Abstract

Anatase TiO$_2$ nanoparticles are successfully synthesized via a simple hydrothermal method with citric acid as a capping agent. The effects of systematic growth periods on the morphological, structural and optical properties of TiO$_2$ nanoparticles are investigated. XRD results confirm the formation of anatase phase while citric acid was used. TEM measurement reveals that the particle size increased by increasing the growth period. TiO$_2$ particles synthesized under different growth periods such as 5, 15, 25 and 45 h are used to prepare a photoanode layer by spray deposition technique for dye-sensitized solar cell fabrication using N719 ruthenium as a sensitizer. It is found that the maximum efficiency (η) of 7.66 % is achieved for 15 h growth period and is attributed to enhanced light harvesting caused by absorption of greater numbers of dye molecules.

1. Introduction

Dye-sensitized solar cells (DSSCs) have been considered as an alternative to semiconductor solar cells due to their good potential and cost effectiveness [1]. It is known that the DSSCs consist of FTO substrate, photoanode material for dye absorption, platinum counter electrode and the electrolyte (iodide/tri-iodide). There are numerous factors which determine the efficiency. Among those, the photoanode is considered to be an important factor for the light harvesting and charge transfer properties. In DSSCs, the semiconductor oxide material with the wide band gap is used as the photoanode material [6]. Titanium-di-oxide (TiO$_2$) gained good attention due to their unique properties such as well matched band alignment with dyes [7]. It is regarded as a promising material preferred as a heterogeneous photo catalyst in solar cells. TiO$_2$ exists in three crystalline polymorphs such as rutile, anatase and brookite. Among those, rutile is the most stable phase, where as anatase and brookite are in metastable phases. However, the anatase phase has been highly employed in wide applications such as DSSCs, photo catalysts, sensors etc. In order to synthesis TiO$_2$ nanoparticles several methods such as sol gel, hydrothermal, laser ablation, solvothermal were adopted. In comparison with the other methods, hydrothermal method is a simple and inexpensive method to prepare well crystalline materials. However, the fast hydrolysis process leads to the formation of irregular phase and morphology. In order to synthesize the nanoparticles without agglomeration, it is necessary to use the capping agent. It is reported that the carboxylic acids have strong affinity towards TiO$_2$ material. The carboxylic acid with a long hydrocarbon chain is considered as an important surfactant for the synthesis of titania nanoparticles. It is very important to identify the capping ligand which offers unique size reduction and better morphology.

In the present work, we report synthesize of anatase TiO$_2$ nanoparticles by facile hydrothermal method, using citric acid as a capping agent. The systematic investigations are carried out for the growth period and the functional properties. The photoanodes are fabricated using spray technique and DSSC performances are studied.

2. Results and Discussion

Figure 1(a) depicts the XRD pattern of the samples at different growth periods of 5, 15, 25 and 45 h. The phase compositions of all the samples were

identified from the XRD pattern. All the diffraction peaks were indexed to (101), (004), (200), (105), (204), (116), (220) and (215) planes of the crystal structure of anatase TiO_2 phase and they matched with card (JCPDS: 21-1272). Whereas the uncapped material shows other planes such as (110) (101) and (211) which corresponded to the rutile phase and mixed with anatase phase. XRD patterns evident that the role of citric acid as a phase directing ligand to obtain only the anatase phase.
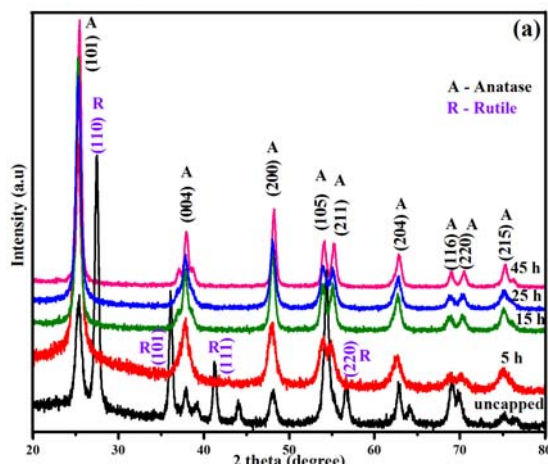

Fig.1(a) XRD pattern of TiO_2 nanoparticles with growth periods of 5, 15, 25 and 45 h.

Figure 1(b) illustrates the Raman spectra of the prepared samples. Generally, the anatase phase has six fundamental vibrational modes such as $[A_{1g} + 2 B_{1g} + 3 E_g]$ and the rutile phase has four fundamental vibrational modes such as $[A_{1g} + B_{1g} + B_{2g} + E_g]$. The citric acid capped nanoparticles grown at different growth period have the four Raman peaks at 148, 400, 158 and 649 cm^{-1} which can be assigned to E_g, B_{1g}, A1g and Eg modes of the anatase phase [2]. The uncapped material has the Raman peaks at 237, 400, 450, 518 and 640 cm^{-1}. Where the peaks 237 and 450 cm^{-1} can be assigned to E_g modes of the rutile phase and the remaining lines belong to the anatase phase as mentioned above. Thus it confirms that the uncapped material has the mixture phase of anatase and rutile. It has good agreement with the XRD data.
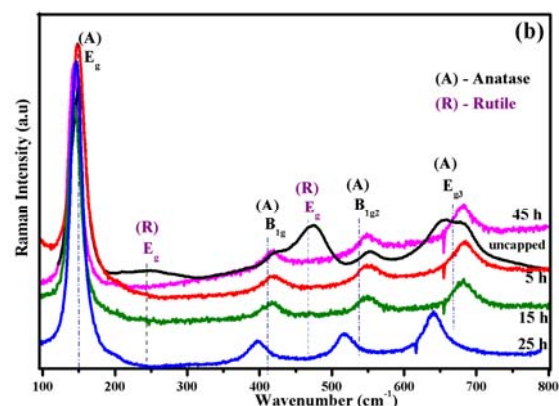

Fig.1(b) Raman Spectrum of TiO_2 nanoparticles with growth periods of 5, 15, 25 and 45 h.

Further confirmation for the electronic levels of the samples was analysed by X-ray photoelectron spectroscopy (XPS). The binding energies obtained in the XPS analysis were corrected by reference to C1s at 284.60 eV. Figure. 2 represents the XPS spectra obtained from Ti and O regions of TiO_2 nanoparticles. Figure 2 (a) shows two strong peaks at 459.5 and 464.9 eV which correspond to the binding energies of Ti $2p_{3/2}$ and Ti $2p_{1/2}$.
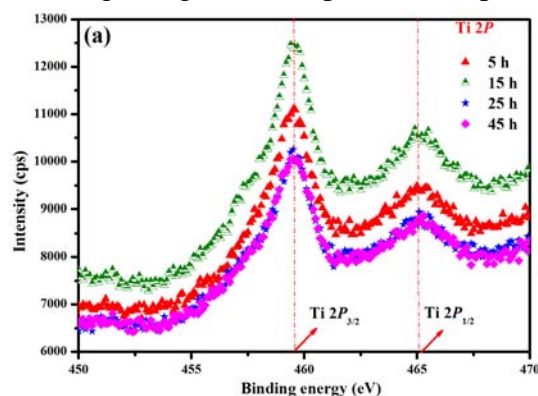

Fig.2(a) XPS spectra of TiO_2 nanoparticles with growth periods of 5, 15, 25 and 45 h.

In Figure 2 (b), there was a strong peak at 530.8 eV, which is attributed to signature of the lattice oxygen O1s in the Ti-O-Ti bonds. All the samples exhibited the similar peak values in the Ti and O core level spectra. No obvious peaks for other elements of impurities were observed.
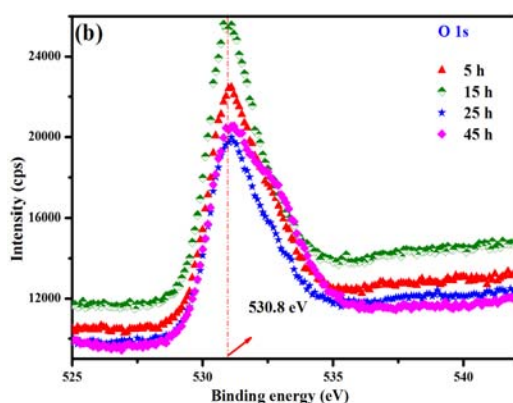
Fig.2 (b) XPS spectra of TiO_2 nanoparticles with growth periods of 5, 15, 25 and 45 h.
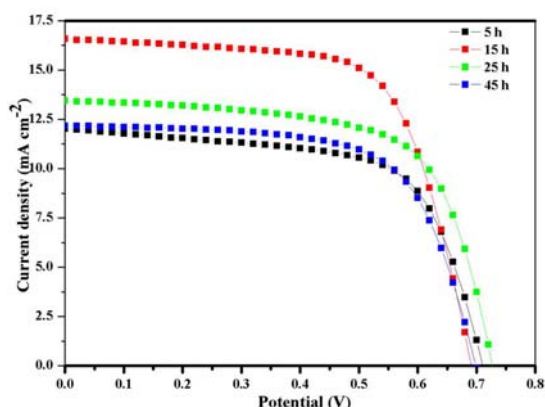

Fig.3 Illustration of I-V characteristics and photocurrent spectra of TiO_2 nanoparticles at growth periods of 5, 15, 25 and 45 h.

Table.1 Device parameters of DSSC

Growth period	5 h	15 h	25 h	45 h
FF	0.64	0.67	0.66	0.65
Eff (%)	5.54	7.66	6.45	5.61
Isc (mA/cm²)	12.02	16.59	13.44	12.16
Voc (V)	0.64	0.69	0.72	0.69

The DSSCs were fabricated using the nanoparticles synthesized at various growth periods. Figure 3 shows the current density versus voltage (I-V) characteristics measured for 5, 15, 25 and 45 h. The values of Voc, Isc, FF and conversion efficiencies (η) of the DSSCs are listed in the Table.1. From the table it is clear that the Voc and FF show somewhat constant whereas the Isc shows an increasing behavior from 12.02 to 16.59 mA cm^{-2} when the particle size increased from 8 - 11 nm (5 h) to 12 - 18 nm (15 h). When the particle size increased as 24 - 29 nm (25 h) and 29 – 37 nm (45 h), the Isc started to drop from 16.59 to 13.44 and 12.16 mA cm^{-2}. The overall conversion efficiency (η) shows the similar behavior of Isc thus the efficiency increased from 5.44 to 7.66% (8 – 11 nm (5h) to 12 - 18 nm (15 h)) and it decreased as 6.45 and 5.61 %. It is clear that the DSSC performance is highly dependent on the Isc factor. When compared with the above data, the growth period 15 h is optimized to yield the maximum efficiency 7.66 % with the particle size of about 12 - 18 nm. The decrease in the efficiency as the particle size increased may be due to the minimal of surface area for the greater absorbance of dye molecules.

3. Conclusions

TiO_2 nanoparticles have been successfully synthesized using facile hydrothermal method. The effect of citric acid on TiO_2 nanoparticles has been studied. The functional properties of the TiO_2 nanoparticles were investigated by TEM, XRD, Raman spectroscopy, UV-vis spectrophotometery, FTIR spectroscopy and XPS analysis. Citric acid promotes the formation of anatase phase through the coordination of carboxylic groups with the titanium complexes. The effects of various growth periods (5, 15, 25 and 45 h) have been investigated. The effect of the photoanode (with various growth periods) on the DSSC conversion efficiency was investigated. It was found that the maximum efficiency (η) of 7.66% was obtained for 15h growth period.

References

[1] O'Regan. B, Gratzel.M. Nature, **353** (1991) 737.

[2] T.Ohsaka,, J. Phys. Soc. Jpn. **48** (1980) 1661.

[3] P.Thistlethwaite, MSHook, Langmuir **16** (2000) 4993.

Synthesis of MoSi$_2$ powder by Molten salt Technique using by MoS$_2$

Daisuke Ishikawa

Graduate School of Engineering, Shizuoka University,
3-5-1 Johoku, Naka-ku, Hamamatsu 432-8561, Japan

Abstract

The hexagonal phase MoSi$_2$ was grown using MoS$_2$ powder as the source material by the molten salt technique. The structural and morphological properties of the resultant silicides are characterized. The layered structure of MoS$_2$ with a hexagonal crystalline structure would affect the growth morphology and enhance the formation of the hexagonal MoSi$_2$. Moreover, Synthesis of the h-MoSi2 was promoted by adding S atom. A simple growth procedure to fix the crystalline structure using an appropriate starting material under a preferable growth environment is proposed.

1. Introduction

Recently, semiconducting silicides, which consist of non-toxic and abundant materials, have attracted much attention for their potential to create new classes of environmentally conscious electronics [1]. The group VI metal silicides are classified in this material group [2]. MoSi$_2$ with stable tetragonal (t-) phases is metallic and has been used in electrode wire materials. On the other hand, the hexagonal (h-) phase MoSi$_2$ has lattice constants of a=0.4622 nm and c=0.6646 nm, and is known to be a narrow gap semiconductor. It is reported that the low temperature phase, h-MoSi$_2$, is expected to be one of the novel silicide semiconductors, which has improved thermoelectric properties [2]. However, the electrical and thermoelectric property of the bulk crystal h-MoSi$_2$ have not been experimentally clarified. Since t-MoSi$_2$ is transformed into h-MoSi$_2$ with the Ti addition by a Mechanical Alloying (MA) technique in the Mo-Ti-Si system [3], it has been reported that Mo-silicides were grown using Mo substrates and Mo-Ti alloy (Mo(Ti)) compacts by the molten salt method. However, the tetragonal phase was formed as well as the hexagonal phase in the silicides. A nonhomogeneous compositional distribution of Mo and Si atoms was observed in the silicides when using the Mo substrate and Mo(Ti) compact [4]. The single phase growth of h-MoSi$_2$ and improved compositional homogeneity of the silicide are required.

On the other hand, MoS$_2$ has a hexagonal structure with lattice constants of a=0.31612 and c=1.22985 nm. The detailed structure of MoS$_2$ and extraordinary chemical properties of the two-dimensional MoS$_2$ nanoclusters are described in Refs.5 and 6, respectively. MoS$_2$ has a characteristic layered structure, i.e., metal chalcogenide slabs are formed by two layers of close-packed chalcogenide atoms sandwiching one metal layer between them. These slabs are stacked with only van der Waals forces between the slabs [7]. It is considered that the use of the thin separated slabs would improve the homogeneity of the atomic distribution in the resultant alloys, because the diffusing species easily can pass through the materials during the treatment. Moreover, it has also been reported that the crystalline structure of the resultant compounds is strongly affected by that of the starting materials. For example, the formation of the zincblende-MnTe phase was demonstrated using ZnTe [8]. Single phase Ca$_2$Si was obtained using Mg$_2$Si as the starting material [9]. In the same manner, it is expected that the h-MoSi$_2$ would be easily obtained using MoS$_2$ as the source material.

In this study, the synthesis of h-MoSi$_2$ was examined using MoS$_2$ powder to overcome the previously mentioned difficulties. The structural and morphological properties of the resultant silicides were also characterized.
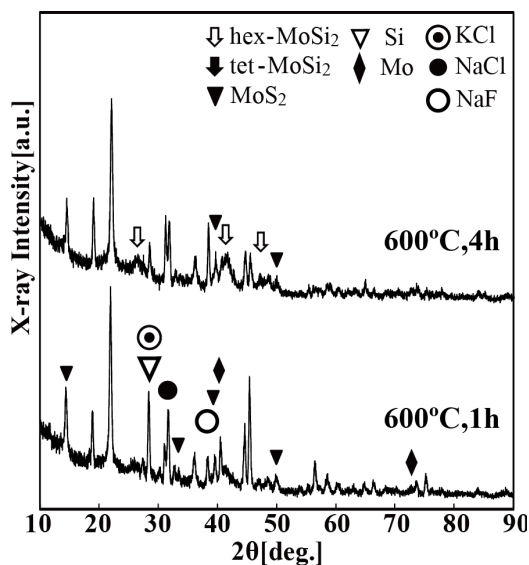
Fig.1 XRD spectra of the resultant powder by using MoS_2 as the source material at 600 ºC.

Fig.2 XRD spectra of the resultant powder by using MoS_2 as the source material at 700 ºC.

2. Experiments

The Mo-silicide powder was synthesized using MoS_2 powder, S powder and a molten salt, comprised of 36.58 mol%NaCl - 36.58 mol%KCl - 21.95 mol%NaF - 4.89 mol%Na2SiF6. The salt mixture, silicon powder (99.999%, 21.85 mol% for the salt mixture), S powder (99.99 %, 10 mol% for salt mixture) and MoS_2 powder (99.9%up, 2.73 mol% for salt mixture) were placed in an SiO2–Al2O3 crucible with the powder. They were thermally treated at 873 and 973K. After the heat treatment, the salt was removed from the sample using deionized H2O. The structural properties of the powder were characterized by scanning electron microscopy (SEM) with energy dispersion spectroscopy (EDS), transmission electron microscopy (TEM) and scanning transmission electron microscopy (STEM) with EDS.

3. Results and Discussion

Figure.1 shows XRD spectra of the resultant powder by using MoS2 as the source material at 600 ºC. The h-$MoSi_2$ was formed with progress of growth time.

Figure.2 shows XRD spectra of the resultant powder by using MoS2 as the source material at 700 ºC. The h-$MoSi_2$ was formed with progress o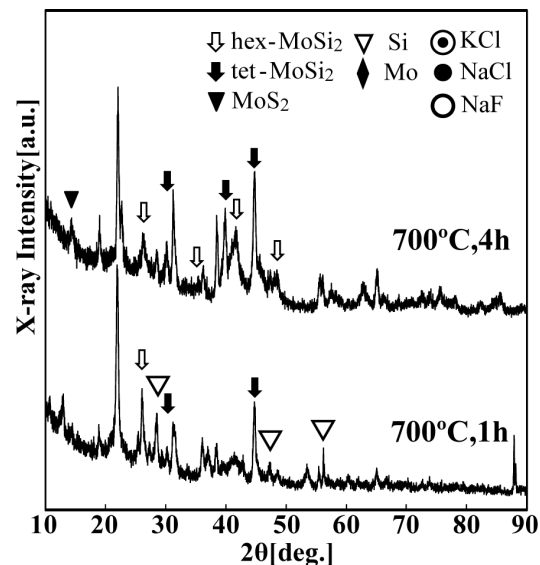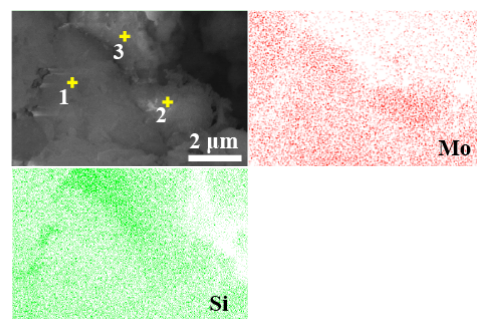f growth time, however, the t-$MoSi_2$ formed as well as h-$MoSi_2$ with progress of growth time. The stable t-$MoSi_2$ was formed at higher temperature.

Source Material	Potision	Composition [at.%]		
		Mo	Si	S
MoS_2	1	25.16	68.73	6.11
	2	17.66	74.92	7.43
	3	-	~100	-

Fig.3 SEM image and corresponding EDS mappings of resultant powders grown using MoS_2 as the source material at 600 ºC / 4h.

Figure.3 shows an SEM image and corresponding EDS mappings of the

resultant powders grown using MoS_2 as the source material. The average composition of the local area on the resultant silicide is approximately Mo : Si ≈ 1 : 2~4. The region with pure Si is also observed. According to the Mo-Si phase diagram, no stable phase exists between $MoSi_2$ and Si [10]. The excess Si is due to the presence of Si powder as the source material.
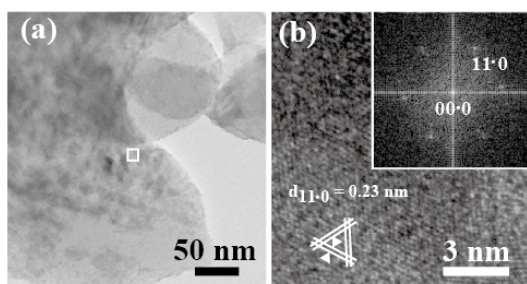

Fig. 4(a) TEM image and (b) an enlarged lattice image of the resultant powder using MoS_2 as the source material at 600 ºC / 4h. The FFT pattern of the images and corresponding crystalline orientations of the domains are shown in the inset.

Figure.4 shows a TEM image and an enlarged lattice image of the resultant powder using MoS_2 as the source material. The Fast Fourier Transformation (FFT) pattern of the images and corresponding crystalline orientations of the domains are shown in the figure. As shown in Fig.4(a), thin silicide films were synthesized, which is due to the layered structure of the MoS_2 starting material. The enlarged lattice fringes show a hexagonal symmetry and the lattice spacing of the fringe is 0.23 nm which corresponds to that of $h-MoSi_2(110)$ as shown in Figure.4(b). The six-fold FFT pattern is consistent with the electron diffraction patterns of the $h-MoSi_2$ observed along the [0001] zone axis.

Figure.5 shows an STEM image and corresponding EDS mappings of one of the powders grown using MoS_2 as the source material. The average chemical composition of the powder is about Mo:Si=1:2, though a small amount of S (~0.4%) remained in the powder.

Figure.6 and 7 shows XRD spectra of the resultant powder by using S and MoS_2 as the source material at 600 and 700 ºC,

respectively. Synthesis of the h-MoSi2 was promoted by adding S powder.
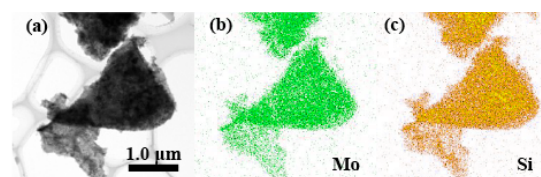
Elements	Composition [at.%]
Mo	12.82
Si	21.46
S	0.36

Fig.5 STEM image and corresponding EDS mappings of one of the powders grown using Mo
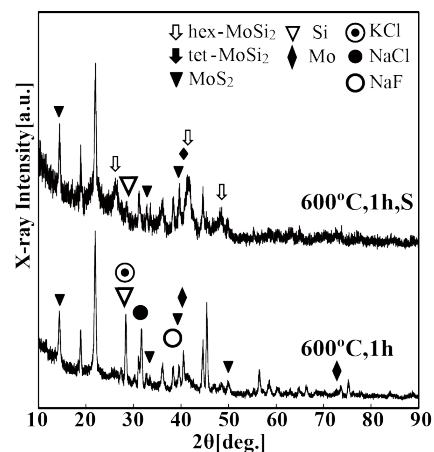

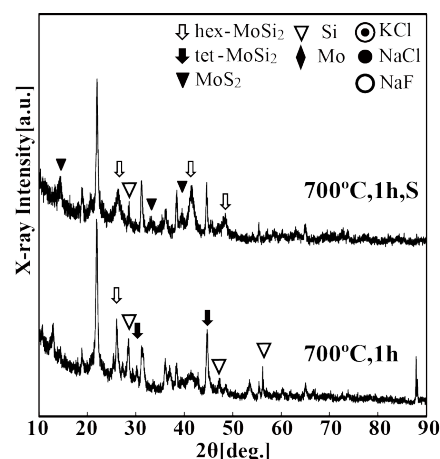Fig.6 XRD spectra of the resultant powder by using S and MoS_2 as the source material at 600 ºC.

Fig.7 XRD spectra of the resultant powder by using S and MoS_2 as the source material at 700 ºC.
.

4. Conclusion

The h-$MoSi_2$ was formed using MoS_2 powder as the source material by the molten salt method. Moreover, thin silicide firms were synthesized, and the composition was uniform. The layered structure of MoS_2 with hexagonal crystals would affect the growth morphology and enhance the formation of h-$MoSi_2$. Synthesis of the h-$MoSi_2$ was promoted by adding S atom. It is expected that this simple growth procedure to fix the crystalline structure using the appropriate starting material under the preferable growth environment would open a new field of silicide semiconducting technology.

Acknowledgements

Reference

[1] APAC-SILICIDE, July 29-31, 2006, Kyoto, Thin Solid Films **515**(22), pp. 8101-8300, edited by Y. Maeda, K.P. Homewood, T. Sadoh, Y. Terai, K. Yamaguchi and K. Akiyama.

[2] T. Nonomura, C. Wen, A. Kato, K. Isobe, Y. Kubota, T. Nakamura, M. Yamashita, Y. Hayakawa and H. Tatsuoka, Physics Procedia **11**, 110 (2011).

[3] A. J. Heron and G. B. Schaffer, Mater. Sci. Eng. A**352**, 105 (2003).

[4] T. Nonomura, C. Wen, K. Shirai, K. Isobe, A. Kato, Y. Kubota, T. Nakamura, Y. Hayakawa and H. Tatsuoka, IOP Conf. Ser.: Mater. Sci. Eng. **18**, 14 (2010).

[5] L. S. Byskov, J. K. Norskov, B.S. Clausen, and H. Topsoe, J. Catal. **187**, 109 (1999).

[6] J. V. Lauriitsen, M. Nyberg, R.T. Vang, M.V. Bollinger, B.S. Clausen, H. Topsoe, K. W. Jacobsen, E. Laegsgaard, J. K. Norskov and F. Besenbacher, Nanotechnology **14**, *385* (2003).

[7] C. F. Castro-Guerrero, F. L. Deepak, A. Ponce, J. Cruz-Reyes, M. D. Valle-Granados, S. Fuentes-Moyado, D. H. Galván and M. Jose-Yacamán, Catal. Sci. Technol. **1**, 1024 (2011).

[8] T. Matsumoto, Y. Souno, H. Tatsuoka, Y. Nakanishi, H. Kuwabara, Appl. Surf. Sci. **169/170**, 325 (2001).

[9] T. Hosono, M. Kuramoto, Y. Matsuzawa, Y. Momose, Y. Maeda, T. Matsuyama, H. Tatsuoka, Y. Fukuda, S. Hashimoto and H. Kuwabara, Appl. Surf. Sci. **216**, 620 (2003).

[10] A.B. Gokhale and G. J. Abbaschian, J. Phase Equilibria **12**, 493(1991).

Synthesis of calcium – Tin system composites by Thermal Annealing

Keisuke Kanda

Faculty of Engineering, Shizuoka University
TEL&FAX : 053-478-1099
E-mail : f0911042@ipc.shizuoka.ac.jp

Abstract

Nanostructured calcium – tin system composites were synthesized by thermal annealing. These shapes of nanostructures grown on surface of composites were different each other. Additionally, formed composites had reactivity against moisture. The structural properties of the resultant composites were characterized by scanning electron microscopy (SEM)

1. Introduction

Recently, a tin and tin compound attracts much attention in various fields. It was reported that tin catalyst was useful for synthesis silicon nanowires [1]. In addition, it was reported that tin oxide nanorods were used as a Li storage compound for Li-ion batteries [2]. Furthermore, it is reported that amorphous zinc tin oxide thin films were examined for thin film transistor application [3].

On the other hand, the intermetallic compounds of the alkali metals with group-IV B elements (Si, Ge, Sn, Pb) from an interesting class of materials, exhibiting quite peculiar crystal structures associated with a variety of chemical-bond types [4]. Among them, Na – Sn phase system has intensively been investigated for more than 80 years[5], the discovery of binary phases and their structural characterization occurred only recently. After the structural characterization of NaSn in 1977[6] it took 20 years until the structures of other binary phases on the tin-rich side were detected and characterized, namely Na_5Sn_{13}(1997)[7], $NaSn_5$(1998)[8], Na_7Sn_{12}(2003)[9], and $NaSn_2$(2005)[10].

In this study, Na-Sn system composites were synthesized by simple thermal annealing method, and their structure property is characterized.

2. Experimental

The composites were synthesized from Sn lumps (Alfa Aesar, -100 mesh, 99.999%) and Ca lumps (High Purity Materials, 99%), which were weighted in an Ar filled glove bag, and charged in boron nitride (BN) crucibles (DENKA; inside diameter, 6 mm; depth, 17 mm). The details of experimental conditions are described in Table 1. Each crucible was sealed in a stainless-steel tube (inside diameter, 13mm; length, 80 mm) to prevent the vaporization of Ca. The sealed tubes were heated at 500ºC for 4 hours in an electric furnace.

The structural properties of the resultant composites were characterized by scanning electron microscopy (SEM).

Table 1 Preparation conditions

Composite	Molar ratio (Na : Sn)
#1	1.0 : 1.0

3. Results and Discussion

Figure 1 shows the SEM image of Composite #1.

Figure 2 shows the SEM image of Composite #1. As shown in Fig.2 (a), a large number of wires were formed on the composite surface. Furthermore, it is interesting that the wires tend to grow up from a lumps formed on the composite surface, which is illustrated by the image in Fig.2(b). Additionally, it is observed that an individual wire is thin, straight, and has a
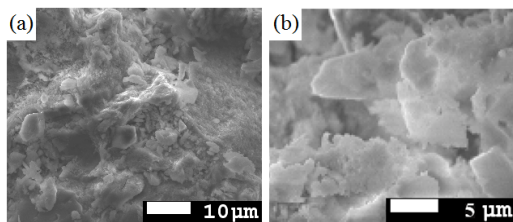
Fig.1 SEM images of Composite #1 shown in Table1.

sharp top end. Meanwhile, it is found that the average diameter of the wires is 400 nm and their lengths are in the range of about 6.7-11μm.

Figure 3 shows the SEM images of Composite #2. As shown in Fig.3 (a), a large number of rods were formed on the composite surface. The average diameter of the rods is 1.76 μm and their lengths are in the range of about 7.7-10μm. Additionally, it is observed that an individual rod has an unhomogeneous shape and has a rugged surface, which is illustrated by the image in Fig.3 (b).

While both composites were stored, both composites reacted with moisture. Therefore, it seems that peaks of compound having a hydroxy group and peaks of monohydrate compound appeared. In other words, it is considered that the nanostructures on the surface of composites were formed by a reaction with the moisture.

Though composite #2 was synthesized under the Sn-rich condition, the peaks of tin of composite #2 is weaker than that of composite #1 from the XRD spectra. However, the XRD spectrum of composite #2 shows surface. On the other hand, the XRD measurement of composite #1 was carried out powder of composite #1. According to XRD spectra, it is considered that most of Sn existed in center of composite #1 and #2.

4. Conclusion

Nanostructured sodium – tin system composites were obtained by simple thermal annealing method. Both composites had reactively against moisture. Additionally, different-shaped nanostructures were synthesized on the surface of both composites. The wires, which are thin, straight, and have sharp top end, were grown in composite #1. On the other hand, the rods, which have an unhomogeneous shape and a rugged surface, were grown in composite #2.

The synthesis condition of Na-Sn system composites is clarified by characterization of the cross-section of composite #1 and #2.

Reference

[1] M. Jeon, K. Kamisako, Mater. Let **63** (2009) 777

[2] Y. Wang, J. Y. Lee, J. Phys. Chem. B **46** (2004) 17832

[3] M. K. Jayaraj, K. J. Saji, K. Nomura, T. Kamiya, H. Hosono, J.Vac.Technol. B **26** (2008) 495

[4] H. Schaefer, B. Eisenmann, W. Muller, Angew. Chem. **85** (1973) 742

[5] W. muller, K. Volk, Z. Maturforsch. **32b** (1977) 709

[6] W. Hume-Rothery, J. Chem. Soc. **131** (1928) 947

[7] J. T. Vaughey, J. D. Corbett, Inorg. Chem. **36** (1997) 4316

[8] T. F. Fassler, C. Kronseder, Angew. Chem. **110** (1998) 1641; Angew. Cem. Int. Ed. **37** (1998) 1571

[9] T. F. Fassler, S. Hoffmann, Inorg. Chem. **42** (2003) 5474

[10] F. Dubois, M. Schreyer, T. F. Fassler, Inorg. Chem. **44** (2005) 477

Synthesis of carbon based materials from organic wastes for dye - sensitized solar cells

R. Karthikeyan[1], M. Navaneethan[2], J. Archana[1], M. Arivanandhan[2] and Y. Hayakawa[2*]

[1]Graduate School of Science and Technology, Shizuoka University
[2]Research Institute of Electronics, Shizuoka University
3-5-1 Johoku, Naka-Ku, Hamamatsu, Shizuoka 432-8011, Japan.
*Email: royhaya@ipc.shizuoka.ac.jp

Abstract

Carbon materials were synthesized from the wastes of organic materials such as corn cob and lemon peel by a simple chemical route. XRD and Raman data indicated that the synthesized materials were related to graphitic based structure with disordered grains. Compared to lemon peel derived carbon, corn cob based carbon material had more ordered structure. FTIR spectra and elemental analysis concluded that the material had oxygen and hydrogen.

1. Introduction

Dye-sensitized solar cells are the third generation electrochemical solar cells, which consist of four different major parts i.e., the photo anode, dye, electrolyte and photo cathode. The typical cell arrangement is shown in Fig. 1. The principle of DSSC's was discussed in 1991 by Gratzel et. al [1]. Photoelectrodes consist of nanostructured TiO_2 particles which are mainly used for photovoltaic conversion. The mechanism of DSSC's is that the dye molecules adsorbed on TiO_2 are exposed to sunlight, as a result photo electrons are generated and are injected into the conduction band of photo anode. The oxidized dye is then reduced by the Iodide (I^-) / tri-Iodide (I^{3-}) electrolyte. Counter electrodes or photo cathodes are utilized for the supply of an electron to the tri-Iodide $[I^{3-}]$ in the reduction process. This cycle should proceed continuously. The overall efficiency depends on every section of DSSC's [2]. High catalytic activity and high cyclic performance depend on the material at the counter electrode. Commercially platinum is used as a best photo cathode. But, in terms of cost and stability, variety of research focuses on the replacement of platinum material without affecting its performance.

Carbon is one of the possible material for overcoming these issues. Because carbon materials are generally considered as a better catalytic material in the field of Fuel cells, supercapactors and so on.
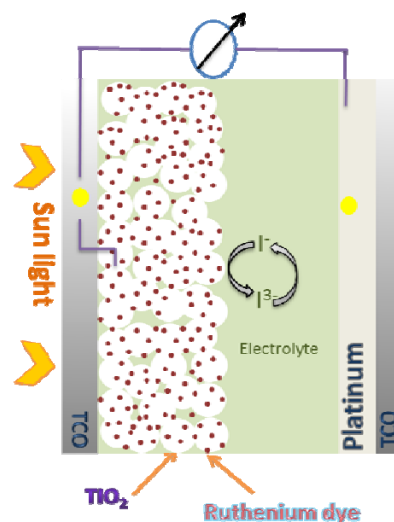

Fig.1 Schematic arrangement of dye-sensitized solar cells

Many research groups have been synthesizing the nanostructured carbon materials as an efficient counter electrode [3]. However, in terms of cost and complicated synthesis methods it finds less attractive towards the application of DSSC's. To overcome the above problems by employing simple and easy synthesis procedures, organic sources are being attracted. In this work synthesis of carbon based materials from the wastes of organics such as corn cob and lemon peel are discussed.

2. Experimental Procedure

Fig. 2 shows the photograph of corn cob waste and lemon peel waste.

2.1. Corn cob carbon synthesis

Phosphoric acid was taken for carbonization as well an activating agent in one step process of chemical synthesis. In our experiment 50 wt.% of phosphoric acid was mixed with the carbon source of 10 g and stirred for 3 h at 120 °C. Residues of the filtrate were sintered at 500 °C in argon atmosphere. The final powder was washed with distilled water several times to maintain the pH in the range of 6 to 7.

Fig. 2 Organic wastes Corn cob and lemon peel.

2.2. Lemon peel carbon synthesis

Potassium hydroxide [KOH] was taken as a corrosive salt for carbonizing as well activating the wastes of lemon peel. The ratio 1:1 of lemon peel and KOH was taken with 100 ml of distilled water. The above mixer was stirred for 3 h at 100 °C. Then the residue was subjected to sintering at 700 °C for 1 h in inert atmosphere. Further washing and filtration were carried out. A solution of 1 M Hcl is added to achieve the pH in the range of 6 to 7.

3. Results and Discussion

Corn cob contains cellulose, hemi-cellulose, and ligno cellulosic organic compounds. During carbonization the unsaturated valences of edge carbon atoms were created because of the removal of other elements from the organic sources. X-ray diffraction image of corn cob derived carbon is shown in Fig. 3. It indicates that graphite based carbon was formed. The two broad peaks at 26° and 44° were related to the (002) and (101) miller indices of graphitic carbon material.
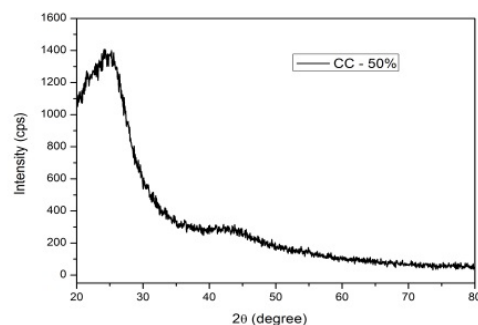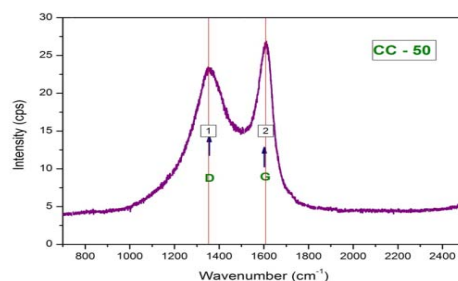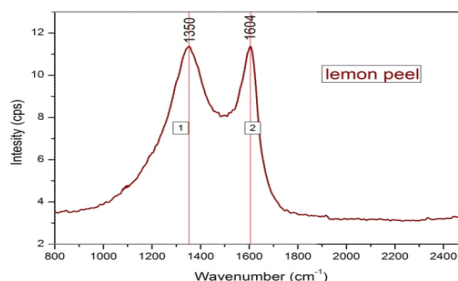
Fig. 3 XRD spectra of corn cob carbon.

Raman spectra of corn cob carbon and lemon peel carbon are shown in Fig. 4 (a) and (b), respectively. The peaks at 1350 and 1604 cm^{-1} were the well known graphite G band and defect D band which related to the graphitic SP^2 -bonding. Lemon peel carbon as well corn cob carbon containd both peaks. But the intensity raio of G and D bands were different. In the case of corn cob carbon, I_G/I_D ratio was 1.27 and for lemon peel carbon the ratio was 1.
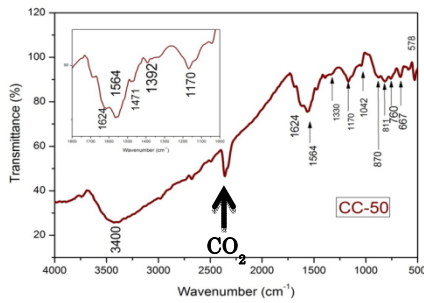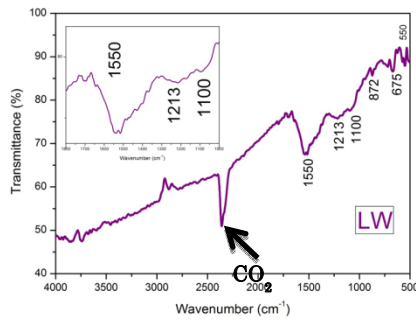
(a)

(b)

Fig 4. Raman spectra of a) corn cob carbon b) lemon peel carbon

The FTIR spectra of the synthesized carbn from corn cob and lemon peel were shown in Fig. 5 (a) (b), respectively. The peak corresponded to 3400 cm^{-1} was related to the O-H vibrations of the hydroxyl groups. The C=C aromatic rings vibration was located at 1564 cm^{-1}. The bands located at 1330 and 1392 cm^{-1} were related to the C-O carboxylate group. Other two peaks at 1170 and 1042 cm^{-1} were due to the C-O stretching vibrations. Peaks at 667 and 578 cm^{-1} were assigned to the out of plane of C-H bending mode. The C-H out of the plane causedanother vibration at 870 and 811 cm^{-1}.

In Fig 5 (b), the strong peak at 1550 cm^{-1} corresponded to the C=C carbon material. The other peaks at 1213,1100 cm^{-1} and 1170, 1042 cm^{-1} were related to C-O bending and stretching modes, respectively. The peak at 872 cm^{-1} was due to the C-H out of plane bending. From the Fig 5, it was found that the presence of carbon and surface oxygen were observed. From both the FTIR spectra peak at 2400 cm^{-1} corresponded to the atmospheric CO_2.

respectively. Fig. 7(a) and (b) indicate the elemental analysis of corn cob carbon and lemon peel carbon, respectively.

From, Fig. 6(a) and Fig. 7(a), it was found that corn cob carbon based carbon contained porous structure with different sizes and approximately 90 at.% of the synthesized material contained carbon and 7 to 8 at.% oxygen. The remaining trace elements of hydrogen, sulfur were present less than 0.5 at.%. Fig. 6 (b) and Fig.7 (b) indicated that three dimensional porous network structure was synthesized from lemon peel carbon. The porous arrangement was ordered throughout the material. It contained 83 at.% of carbon , 14 to 15 at.% of oxygen and remaining of trace elements.
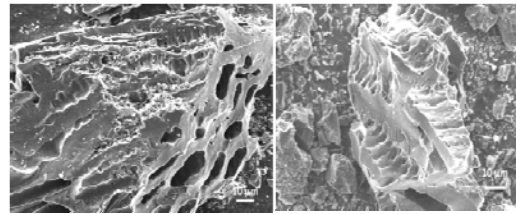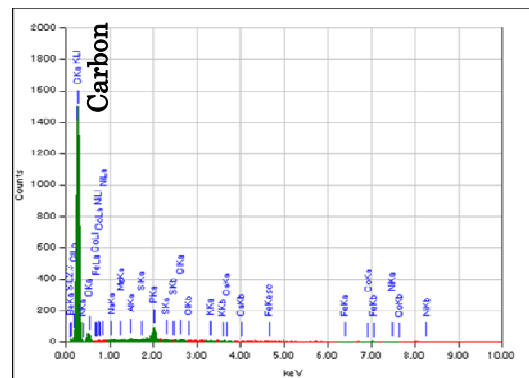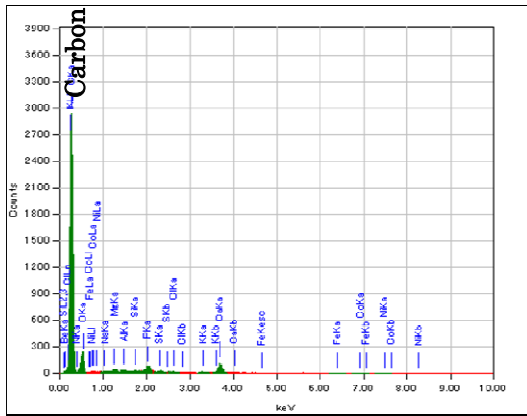

(a)
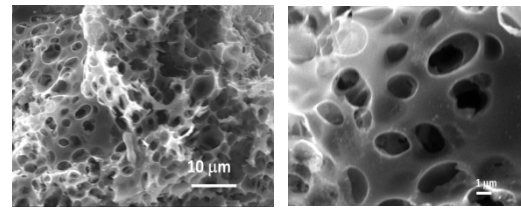
(b)

Fig. 6 FESEM images of (a) corn cob carbon (b) lemon peel carbon

(a)

Fig. 5 FTIR spectra of (a) corn cob carbon and (b) Lemon peel carbon

(a)

FESEM images of corn cob and lemon peel carbon are shown in Fig. 6(a) and (b),

(b)

Fig 7 Elemental analysis of corn cob carbon
(a) lemon peel carbon (b)

4. Conclusion

Synthesis of carbon based material from the organic wastes such as corn cob and lemon peel were performed. From the XRD it is clear that material related to graphitic based structure with disordered grains. Raman spectra explains that the amount of graphitic based carbon and its disorderness. Compared to lemon peel derived carbon, corn cob based carbon material has a more ordered structure, which can be understood from the ratio of I_G/I_D. FTIR spectra and elemental analysis conclude that the material has oxygen and hydrogen, adsorbed from the atmosphere. The synthesized material of highly activated carbon can be utilized further as a counter electrodes for dye sensitized solar cells.

Acknowledgement

References

1. O'regan, B. & Gratzel, M. Nature **353**,737-740 (1991).
2. Brian E. Hardin, Henry J. Snaith and Michael D. McGehee Nature Photonics **6**,162-169 (2012).
3. Won Jae Lee, Eswaramoorthy Ramasamy, Dong Yoon Lee and Jae Sung Song Applied materials and interfaces **6** 1145-1149 (2009).

Growth of CaSi2 layers on Si (111) substrates

Natsuki Kurebayashi

Faculty of Engineering, Shizuoka University
3-5-1 Johoku, Naka-ku, Hamamatsu, Shizuoka 432-8561, Japan
TEL&FAX: +81-53-478-1099
E-mail: f0711059@ipc.shizuoika.ac.jp

Abstract

CaSi2 to generate a thin film onto the Si(111) substrate in an atmosphere of Ca by vapor deposition. Growth time becomes longer, began to increase in the proportion of Ca component of the substrate surface. The structural properties of the resultant composites were characterized by scanning electron microscopy (SEM), energy dispersive x-ray spectroscopy (EDS), and X-ray diffraction (XRD).

1. Introduction

First, I will introduce silicon-based nanosheet structure. Nanosheet is a nanomaterials with nanometer-scale thickness obtained apart by a layer constituting the layered compound, the horizontal size of the micrometer scale.[1]

There are the typical ones that are made graphene in the current characterization studies, and have been functionalized. Such as high thermal conductivity and high carrier mobility, as has been reported characteristics are those of good quality[2]

Those are expected to apply wiring material, such as to chemical and bio-sensors. As with graphene with silicon nanosheet effective properties can be expected. Considered trying to produce silicon-based nanosheet structure, and can be used as a starting material, which is a layered crystal CaSi2 as a preliminary step.[3]

CaSi2 layered crystal structure is a Ca atomic layer is inserted between the plane Si(111) diamond-shaped. High vapor pressure Ca, re-evaporation of calcium occurs in the silicide formation temperature, it is difficult silicide growth. Toxicity rather than Ca, both Si, it is a material with low environmental impact because it is an abundant element in the Earth's crust.[4]

As mentioned earlier in a high vapor pressure Ca, in the silicide formation temperature growth is difficult because the evaporation will occur again.[5]

Thus, the purpose of this study is on the growth of CaSi2 layers on Si(111) substrates in an atmosphere of Ca using a quasi-closed tube container and, the observation and composition analysis of the surface structure of those compounds.

2. Experimental

It was grown by vapor phase growth of CaSi2. The composites were synthesized from Ca powder (0.05g, particle size :1-3mm) and Si substrate (0.03g). The inside of the chamber is evacuated to about 10^{-3}Pa degree of vacuum, heat-treated at 600 ℃ Growth time I was done in 2.5 hours and 2.0 hours and 1.5 hours.

The structural properties of the resultant composites were characterized by scanning electron microscopy (SEM), energy dispersive x-ray spectroscopy (EDS), and X-ray diffraction (XRD).

3. Results and Discussion

Fig.1 shows SEM images of each samples of the surface of the substrate by the growth time.
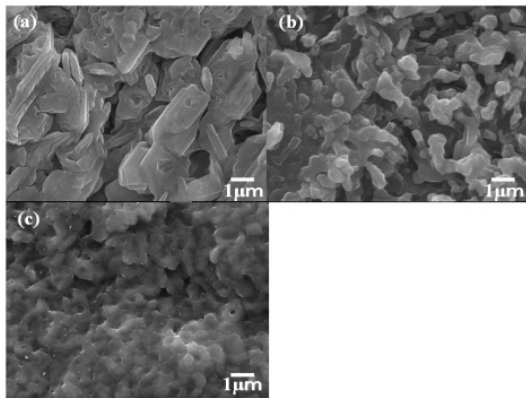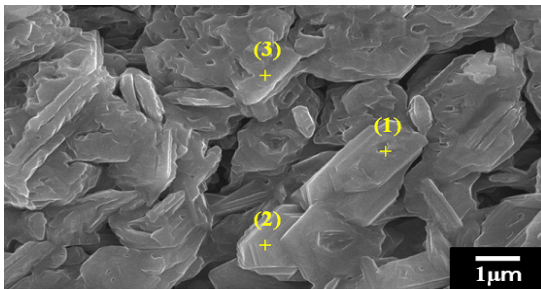
Fig.1 SEM images of each sample.
(a) 1.5h (b) 2.0h (c) 2.5h

Growth time of all, I look in particular at 1.5 hours, as have grown big piled plate-like crystals. The size of the plate is seem growth time becomes longer and smaller. Crystals in 2.5 hours is quite small, it is seem to be the membrane.
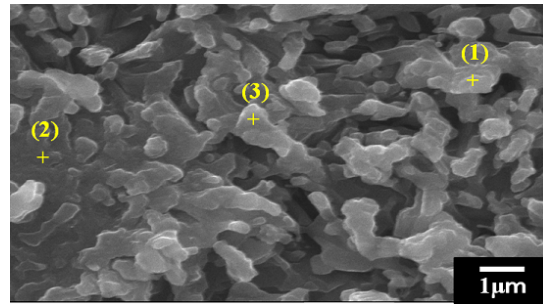

Table.2 the results of EDS substrate surface growth time 2.0 hours.

Position at(%)	Ca	Si	C
1	40.34	49.40	10.25
2	42.17	49.23	8.59
3	38.43	51.89	9.57

Position at(%)	Ca	Si	C
1	30.67	48.80	20.53
2	28.72	53.27	13.60
3	34.28	52.95	12.77

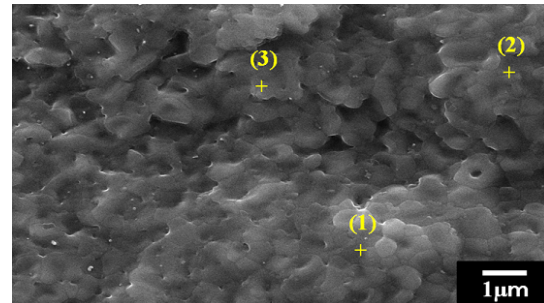Table.1 the results of EDS substrate surface growth time 1.5 hours.

Table 1 shows the results of EDS substrate surface growth time 1.5 hours. The composition ratio of Ca and Si was approximately 3:5 in all points.

Table 2 shows the results of EDS substrate surface growth time 2.0 hours. The composition ratio of Ca and Si was approximately 4:5 in all points. It has increased the proportion of Ca than 1.5 hours was observed.

Position at(%)	Ca	Si	C
1	63.70	28.69	7.61
2	65.28	28.58	5.88
3	64.53	27.28	8.19

Table.3 the results of EDS substrate surface growth time 2.5 hours.

Table 3 shows the results of EDS substrate surface growth time 2.5 hours. The composition ratio of Ca and Si was approximately 2:1 in all points. It has further increased the proportion of Ca from the results of 2.0 hours.

Based on the results of EDS, I have observed the XRD spectra of the sample substrate surface obtained by heat treatment of the composition ratio was close to 1.5 times the most $CaSi_2$. These are shown in Fig.2.
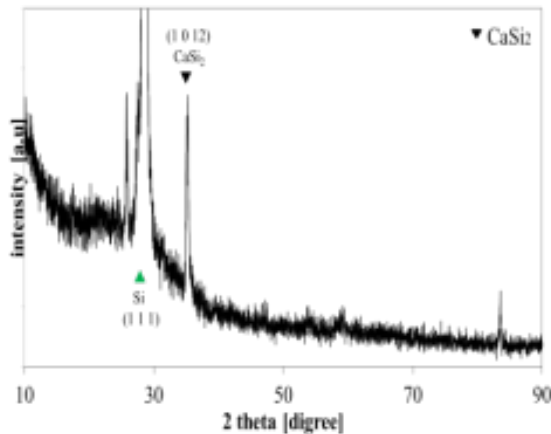
Fig.2 the XRD spectra of the substrate surface of the sample obtained by heat treatment for 1.5 hours.

The diffraction peaks of CaSi2 were observed. And also, this most biggest perk is silicon. This result is believed, by performing a heat treatment for 1.5 hours in vacuo, and CaSi2 is generated on the substrate surface.

4. Conclusion

In this study we have conducted observations of the surface structure of the compounds obtained, the composition analysis, and attempts film growth CaSi2 onto Si(111) substrate in an atmosphere of Ca with the container closed tube level. Growth time becomes longer, began to increase in the proportion of Ca component of the substrate surface. The results of the EDS, the substrate surface of the sample generated by the growth time 1.5 hours, it was possible for making the composition ratio of Si and Ca is the most close to 1:2. From XRD spectrum of the sample is considered generated by the growth time of 1.5 hours in vacuum, to have been generated on the substrate surface CaSi2.

References

[1] T. Yui, Y. Mori, T. Tsuchino, T. Itoh, T. Hattori, Y. Fukushima and K. Takagi, Chem. Mater. 17 (2005) 206.

[2] M. Muramatsu, K. Akatsuka, Y. Ebina, K. Wang, T. Sasaki, T. Ishida, K. Miyake and M. Haga, Langmuir **21** (2005) 6590.

[3] A.S. Heintz, M.J. Fink, B.S. Mitchell, Adv. Master, 19 (2007) 3984.

[4] S.Y. Jeong, J.Y. Kim, H.D. Yang, B.N. Yoon, S.-H. Choi, H.K. Kang, C.W. Yang, Y.H. Lee, Adv. Master, 15 (2003) 1172.

[5] J.-C. Gabriel, F. Camerel, B. Lamairem, H. Desvaux, P. Davidson and P. Batail, Nature 413 (2001) 504

Study of the substrate treatment effect on initial growth of Ti-Oxide Nanorods by Thermal Oxidation

Tomoji Matsushita

Graduate School of Engineering, Shizuoka University,
3-5-1 Johoku, Naka-ku, Hamamatsu, Shizuoka 432-8561, Japan
TEL&FAX: +81-53-478-1099
e-mail: f0130151@ipc.shizuoika.ac.jp

Abstract

The titanium oxide nanorods on titanium wire were grown by the thermal oxidation technique in the air. The pretreatment dependence of nanorods was investigated. The length and the diameter of nanorods grown on the substrate chemically-etched in hydrochloric acid by the thermal oxidation at 800 ºC for 4 hours were approximately 1300 nm and 190 nm, respectively. Layer and nanorods were composed of Ti-oxide such as TiO_2 rutile. It is clarified that the length and diameter of nanorods depend on pretreatment.

1. Introduction

TiO_2 is an n-type semiconductor with wide band gap energy of 3.0-3.2 eV and has been widely used for various applications in dye-sensitized solar cells [1], gas sensors [2], photocatalyst [3] and negative electrode for lithium rechargeable batteries [4].

Nanostructured materials have attracted much attention for its promising potential for electronics, optoelectronics applications because they have many merits such as a high surface to volume ratio and short and controlled electron pathway [5]. They have been reported in various forms such as nanotubes [6], nanowires [7], nanoparticles [8] and nanoplates [9].

TiO_2 nanostructures are synthesized by many techniques such as sol-gel method [10], hydrothermal process [11], electrochemical oxidation method [6] and thermal oxidation technique [12]. Among of them, thermal oxidation technique is simple and cheap. TiO_2 nanostructures grown by this technique was carried out under carrier gas such as acetone [7] and ethanol [12]. However, almost none of this technique is able to grow the TiO_2 nanostructures in the air.

In this study, we reported the growth of Ti-oxide nanorods by thermal oxidation technique of titanium substrates in the static air. In addition, the pretreatment dependence of nanorods was investigated.

2. Experiments

The TiO_2 nanorods were grown by thermal oxidation technique of titanium substrates in the air. Titanium wires with diameter of 1 mm were used as the substrates. The substrates were polished by three pretreatment methods. The pretreatment methods were mechanical polish with #400 and #1500 sandpapers, chemical etching in hydrochloric acid at 80 ºC for 1 min and chemical etching in sulphuric acid at 80 ºC for 1 min. And then, the substrates were ultrasonic cleaned in acetone and ethanol for 10 min. The substrates were placed at the center of electric furnace. The temperatures were raised to 800 ºC for 1 hour. The substrates were annealed in the air for 4 hour. The temperatures were reduced to room temperature in atmosphere.

The Ti-oxide nanorods were characterized by field emission scanning electron microscopy (FE-SEM, JSM-7001F) and X-ray diffraction methods (XRD, RINT Ultima III).

3. Results and Discussion

Figure 1 shows SEM images of the substrate polished by three pretreatment methods. Figure 1(a), 1(b) and 1(c) show
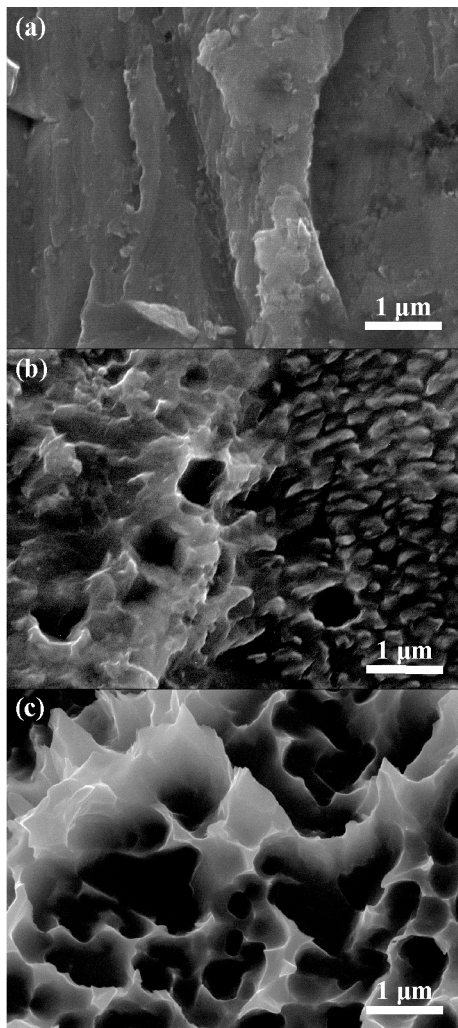
Fig. 1. SEM image of the substrate (a) polished with #400 and #1500 sandpaper, (b) chemically etched by hydrochloric acid, (c) chemically etched by sulphuric acid.

SEM images of the substrate polished with #400 and #1500 sandpapers, chemically etched in hydrochloric acid and chemically etched in sulphuric acid, respectively. In Fig. 1(a), 1(b) and 1(c), the surface of substrate were different. In Fig. 1(a), the surface of the substrate polished with #400 and #1500 sandpapers is rough. In Fig. 1(b), on the substrate chemically etched in hydrochloric acid, many ledges were formed. The diameter of ledges was approximately 200 nm. In Fig. 1(c), on the substrate chemically etched in sulphuric acid, many voids were formed. The diameter of voids was submicron order.
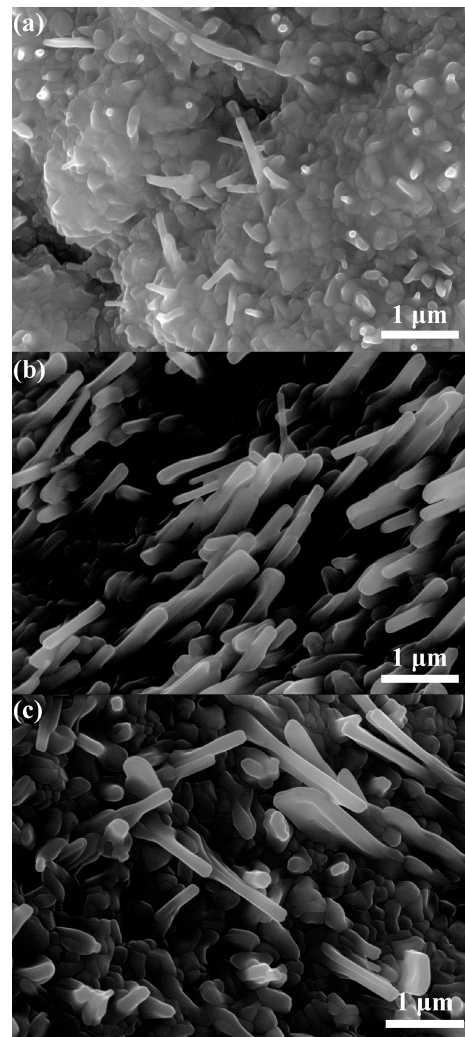

Fig. 2. SEM image of Ti-oxide layer and nanorods on the substrate (a) polished with #400 and #1500 sandpaper, (b) chemically etched by hydrochloric acid and (c) chemically etched by sulphuric acid.

Figure 2 shows SEM images of TiO_2 nanorods grown at 800 ºC for 4 hours. In Fig. 2(a) and 2(c), nanorods were formed and laid randomly on the layer. In Fig. 2(a), the length and the diameter of nanorods were approximately 910 nm and 130 nm, respectively. In Fig. 2(c), the length and the diameter of nanorods were approximately 1400 nm and 190 nm, respectively. In Fig. 2(b), aligned nanorods were formed and laid on the layer. In Fig. 2(b), the length and the diameter of nanorods were approximately 1300 nm and 190 nm, respectively. The length and the diameter of nanorods in Fig. 2(b) was formed as same as that in Fig. 2(c).
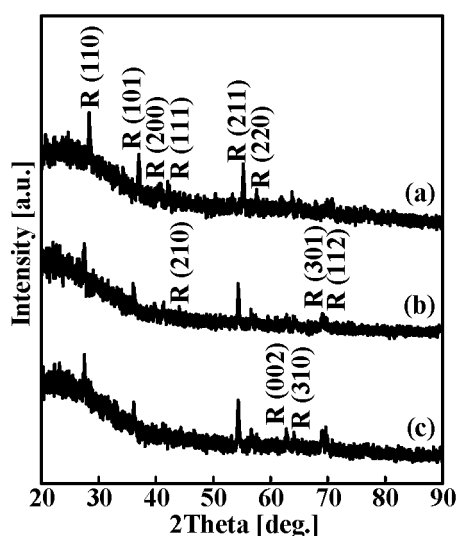
Fig. 3. XRD spectra of Ti-oxide layer and nanorods on the substrate (a) polished with #400 and #1500 sandpaper, (b) chemically etched by hydrochloric acid and (c) chemically etched by sulphuric acid. R represents TiO_2 rutile structure.

However, the density of nanorods in Fig. 2(b) was more than that in Fig. 2(c).

Figure 3 shows XRD spectra of TiO_2 nanostructures grown at the temperature of 800 ºC for 4 hours. TiO_2 exist in three forms of tetragonal rutile, tetragonal anatase and orthorhombic brookite. In Fig. 3, some diffraction peaks of TiO_2 rutile were observed. Overlapped diffraction peaks due to other TiO_2 structures and Ti-oxide materials such as TiO, Ti_2O_3 and Ti_3O_5 were observed in Fig. 3(a). Hence, layer and nanorods in Fig. 2(a) were composed of Ti-oxide such as TiO_2 rutile.

4. Conclusions

Ti-oxide nanorods were grown by thermal oxidation technique in the air at 800 ºC for 4 hour. Aligned nanorods were formed and laid on the layer on the surface chemically-etched by hydrochloric acid. Layer and nanorods were composed of Ti-oxide such as TiO_2, TiO, Ti_2O_3 and Ti_3O_5.

Reference

[1] S. Dai et al., Sol. Energy Mater. Sol. Cells **84** (2004) 125.

[2] L. Francioso et al., Sens. Actuat. B **130** (2008) 70.

[3] M. Muruganandham et al., Sol. Energy Mater. Sol. Cells **81** (2004) 439.

[4] C. Natarajan et al., Electrochim. Acta. **43** (1998) 3371.

[5] Y. Xia et al., Adv. Mater. **15** (2003) 353.

[6] X. Zeng et al., J. Alloys Compd. **509** (2011) L221.

[7] K. Huo et al., J. Nanosci. Nanotechnol. **9** (2009) 3341.

[8] H.-D. Jang et al., Ultramicroscopy **108** (2008) 1241.

[9] H. G. Yang et al., J. AM. CHEM. SOC. **131** (2003) 4078.

[10] Y. Lei et al., Appl. Phys. Lett. **78** (2001) 1125.

[11] R. Yoshida et al., J. Solid State Chem. **178** (2005) 2179.

[12] S. Daothong et al., Scripta Mater. **57** (2007) 567.

Structural Characterizations of Ag Nanostructures on Various Metallic Substrates

Meng Erchao

Graduate School of Science and Technology, Shizuoka University,
3-5-1, Johoku, Naka-ku, Hamamatsu, Japan
TEL&FAX : 053-478-1099
E-mail : f5145034@ipc.shizuoka.ac.jp

Abstract

Various Ag nanostructures were grown on metallic substrates using hexakisphosphate (IP6) as a silver carrier agent. The structural and morphological properties of the Ag nanostructures were characterized by SEM, EDS and XRD. SEM images shown that roughly three types of Ag nanostructures were grown on different metallic substrates. EDS and XRD measurements shown that the resultant nanostructures were silver. The growth mechanism of various Ag nanostructures on metallic substrates was discussed.

1. Introduction

In recent years, silver has been extensively investigated for its catalytic activities [1], anti-microbial activities [2], and used to avoid infections and prevent spoilage. Many researchers have focused on the anti-bacterial, ability to kill microorganisms and multi-functional properties of silver nano-particles [3–5]. Various methods have been employed for nano-silver production, and the syntheses of various shapes of Ag nanostructures have been reported, such as dendrite [6,7], wire [8], irregular-shaped wire [9], chain-like [10] and particle [11] structures.

For practical uses, it is important to fabricate the nanostructures using a simple process with low costs. The systematic synthesis study is also important to clarify the growth mechanism for various shaped Ag nanostructures. In addition, the structural and morphological controlling of the nanostructures is also required to enhance the functional properties for specific applications.

In this study, a variety of Ag nanostructures were synthesized on various metallic substrates, and hexakisphosphate (IP6) [12–14] was used as a silver carrier agent. Moreover, the growth mechanism of Ag nanostructures on various metallic substrates was discussed.

2. Experiments

Ag nanostructures were grown on various metallic substrates using the LS21 solution consisting of Ag-IP6. The experimental process is as follows, as shown in Fig 1. A drop of the solution was dripped onto metallic substrates, then kept in air for several minutes at room temperature. Then the solution was immediately dried using a gas burner or hot plate. When the sample was dried, Ag nanostructures appeared on the surface of metallic substrate.

The structural and morphological properties of the Ag nanostructures were characterized by scanning electron microscopy (SEM) along with energy dispersive X-ray spectroscopy (EDS), X-Ray Diffraction (XRD).
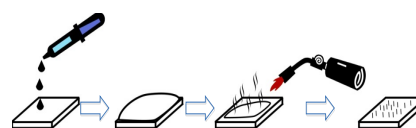

Fig 1 the experimental process of Ag nanostructures grown on metallic substrates

In addition, the surface condition of the Ag nanostructure and dried IP6 complexes was characterized by X-ray photoelectron spectroscopy (XPS) using a VG, ESCA-LAB Mk II with a non-monochromatized Al Kα source (hν = 1486.6 eV). The energy calibration for a charge correction in the spectra was made using the C1s peak.

3. Results and Discussion

Figure 2 shows the SEM images of a variety of nano-, and micro-structures grown on various kinds of metallic substrates. As shown in Fig 2, dense Ag nanostructures were formed on (a) Cu, (b) Mn and (c) CaSi2 substrate. However, low density distribution of Ag structures are observed on (d) Fe, (e) Ti, (f) Al, (g) SrSi2, (h) Mo and (i) W substrates.
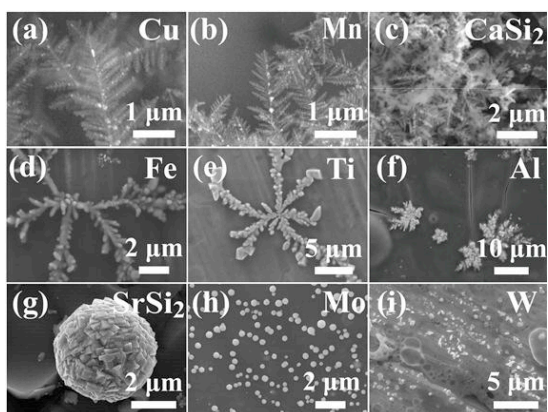
Figure 2. A variety of Ag nanostructures grown on various kinds of metallic substrates.

As shown in Figure 2, roughly speaking, three types of Ag nanostructures are grown. One is the dendrite structure, as shown in figures (a) – (c). It is also observed that the three-dimensional Ag dendrite structures are grown on (a) Cu and (b) Mn substrates. However, the two-dimensional Ag dendrite structures are grown on (c) CaSi$_2$ substrate. For cases (d) – (f), the fractal-shaped structures are dominantly observed. In addition, the particles are formed on the (g) SrSi$_2$, (h) Mo and (i) W substrates.

A variety of Ag nanostructures were simply fabricated using Ag-IP6 on the various types of metallic substrates. It is interesting that the growth morphology of the nanostructures depends on the metallic substrate materials. The discussion on the substrate metal dependence of the morphology and the growth mechanism will be discussed later.
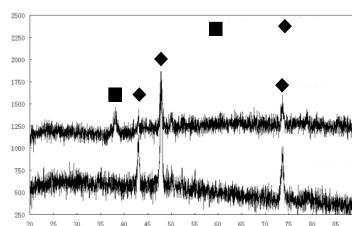
Fig 3 the XRD patterns of Ag nanostructures on Mn substrate

Fig 3 is the XRD patterns of Ag nanostructures on Mn substrate. And the XRD pattern of the Mn substrate is shown in Fig 3 for comparison. The figure shows that the peak of Ag is detected, which indicates that the nanostructures grown on Mn substrate is Ag.

So far, many mechanisms have been discussed on the growth of Ag nanostructures. In this study, Ag is from Ag-IP6. When the LS21 solution is dripped on the metallic substrate, the metallic atoms react with Ag-IP6, and Ag ions are released into solution, which provides Ag ions to form the Ag nanostructures.

Some references reported that the transition of the dendrite to the fractal structures is caused by the density of the deposited atoms in the solution. The existence of the dense deposited atoms and anisotropic growth leads to the formation of the dendritic structures, and a low density of deposited atoms leads to the formation of the fractal structures [15 – 18]. Therefore, the deposition rate and silver ions concentration are very important to the structural control of Ag structures.
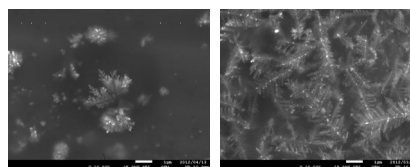
Fig 4 SEM images of the Ag nanostructure grown on (a) Al substrate and (b) Cu substrate
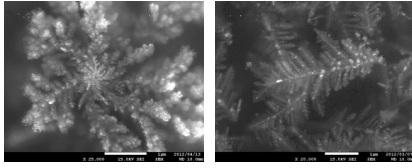
Fig 5 High magnification SEM images of the Ag nanostructure grown on (a) Al substrate   and   (b) Cu substrate

Fig 4 and Fig 5 are the low-magnification and high-magnification SEM   images of the Ag nanostructures grown on Al substrate and Cu substrate, respectively. These two figures shown a low density of fractal Ag nanostructures are obtained on Al substrate. For the Cu substrate, the dense dendrite Ag nanostructures are grown on the surface.

Based on the previous discussion, the substrate metal dependence of the grown Ag structures is caused by the reaction between Ag-IP6 and the substrate metals. For the Cu substrate, Ag-IP6 significantly reacted with the Cu atoms of the substrate, and the Ag atoms are supplied from the Ag-IP6 solution to form the dense Ag nanostructures. While for the Al substrate, the reaction of Ag-IP6 with the Al substrate is not very active. Thus, the low density of Ag-IP6 reacted with the Al substrate to form the low density Ag nanostructures.

In order to demonstrate this mechanism, the XPS spectra are carried out. Figures 6 (a) and (b) show the Ag(3d) and Cu(2p) XPS spectra of the dried metal-IP6 complexes after the reaction with the Cu substrate, respectively. Figures 6 (c) and (d) show the Ag(3d) and Al(2p) XPS spectra of the dried metal-IP6 complexes after the reaction with the Al substrates. As references, the Ag(3d) XPS spectrum of the originally dried IP6, and Cu(2p) and Al(2p) XPS spectra of the Cu and Al substrates, respectively, are also shown.

As shown in Fig. 6 (a), the intensity of the Ag XPS spectra of the treated dried metal-IP6 is significantly reduced compared to that of the untreated Ag-IP6, which shows that the Ag atoms are removed from the Ag-IP6 by the treatment. On the other hand, the shape of the Cu(2p) spectrum is significantly changed compared with to that of the untreated Cu substrate, which means that the Cu atoms

have combined with IP6 to form the metal-IP6 complexes, as shown in Fig. 6 (b). The intensity of the Ag XPS spectra of the treated and dried metal-IP6, as shown in Fig.6 (c), is slightly reduced compared with that of the untreated Ag-IP6, which shows that some of the Ag atoms have been removed from the Ag-IP6 by the treatment. On the other hand, the intensity of the Al(2p) spectrum is quite low compared with that of the untreated Al substrate, as shown in Fig. 6 (d), which means that Al atoms are only slightly replaced by Ag atoms to combine with IP6 in the solution. The XPS results agree with the previous discussion.
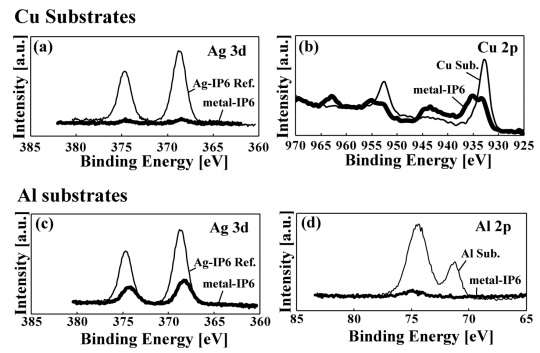

Fig 6 . (a) Ag(3d) and (b) Cu(2p) XPS spectra of dried metal-IP6 complexes after the reaction with the Cu substrate. (c) Ag(3d) and (d) Al(2p) XPS spectra of dried metal-IP6 complexes after the reaction with the Al substrates. As references, Ag(3d) XPS spectrum of originally dried IP6, and Cu(2p) and Al(2p) XPS spectra of the Cu and Al substrates are also shown.

Therefore, the metallic substrates dependence of Ag nanostructrues is summarized. When Cu, Mn, CaSi2 react with Ag-IP6, higher deposition rate and silver ion concentration are provided, which introduces Ag dendrite structures growth. Fe, Ti, Al cause the low deposition of Ag, thus the fractal shaped Ag structures are formed. For W, Mo and SrSi2,   the reaction of IP6 with these substrates rarely take place, thus , particles are synthesized.

4. Conclusions

It was demonstrated that various kinds of Ag nanostructures were prepared using IP6 on various metallic substrates. The dendrite

structures on Cu, Mn and CaSi$_2$, the fractal structures on the Fe, Ti and Al substrates, the particles on Mo, SrSi$_2$ and W were controllably obtained. It is noted that the IP6 plays an important role as a silver carrier agent for the structural and morphological control of the Ag nanostructures. It is expected that this simple and easy nanostructure fabrication technique using metal complexes will encourage us to further develop sophisticated materials.

Acknowledgments

Reference

[1] M. H. Rashid and T. K. Mandal, J. Phys. Chem. C, 111, 16750-16760 (2007)

[2] V. K. Sharma and R. A. Yngard, Y. Lin, Adv. Coll. Int. Sci., 145, 83-96 (2009)

[3] R. Dastjerdi and M. Montazer, Colloids and Surfaces B: Biointerfaces, 79, 5-18 (2010)

[4] A. Pourjavadi and R. Soleyman, Mat. Res. Bull., 46, 1860-1865 (2011)

[5] D. V. Quang, P. B. Sarawade, A. Hilonga, J.-K. Kim, Y. G. Chai, S. H. Kim, J.-Y. Ryu and H. T. Kim, Colloid Surf. A-Physicochem. Eng. Asp., 389, 118-126 (2011)

[6] X. Qin, Z. Miao, Y. Fang, D. Zhang, J. Ma, L. Zhang, Q. Chen and X. Shao, Langmuir, 28, 5218-5226 (2012)

[7] J. Fang, H. Yu, P. Kong, Y. Yi, X. Song and B. Ding, Cryst. Growth Des., 7, 864-867 (2007)

[8] S. Kundu, D. Huitink, K. Wang and H. Liang, J. Coll. Int. Sci., 344, 334-342 (2010)

[9] X.-J. Zheng, Z.Y. Jiang, Z.-X., Xie, S.-H. Zhang, B.-W. Mao and L.-S. Zheng, Electrochem. Comm., 9, 629-632 (2007)

[10] G. Wei, C.-W. Nan, Y. Deng and Y.-H. Lin, Chem. Mater., 15, 4436-4441 (2003)

[11] B. An, X.-H. Cai, F.-S. Wu and Y.-P. Wu, Trans. Nonferrous Met. Soc. China, 20, 1550-1554 (2010)

[12] U. P. R.-Filho, S. Var Jr., M. P. Felicissimo, M. Scarpellini, D. R. Cardoso, R. C. J. Vinhas, R. Landrs, J. F. Schneider, B. R. McBarvey, M. L. Andersen and L. H. Skibsred, J. Inorg. Biochem., 99, 1973-1982 (2005)

[13] Z. He, W. Honeycutt, T. Zhang and P. M. Bertsch, J. Environ. Qual., 35, 1319-1328 (2006)

[14] Z. He, C. W. Honeycutt, T. Zhang and P. M. Bertsch, Soil Sci. Soc. Am., 35, 1319-1328 (2006)

[15] M. Uwaha and Y. Saito, J. Cryst, Growth, 99, 175-178 (1990)

[16] H. Brune, C. Romainczyk, H. Röder and K. Kern, Nature, 369, 469-471 (1994)

[17] V. V. Agrawal, G. U. Kulkarni and C. N. R. Rao, J. Coll. Int. Sci., 318, 501-506 (2008)

[18] Y. Sawada, A. Dougherty and J. P. Gollub, Phys. Rev. Lett., 56, 1260-1263 (1986)

Characterizations of Sodium Carbonate and Stannate Nano-/Micro-rods

Kaito Nakane

Graduate School of Engineering , Shizuoka University
TEL&FAX : 053-478-1099
E-mail : f0230119@ipc.shizuoka.ac.jp

Abstract

Carbonate, stannate and silicate materials with various structures were fabricated by a simple experimental process. The molar ratio of Na：Sn affects the composition and structural property of the sodium compound. Moreover, the structural property of sodium silicate was affected by the growth temperature. The structural properties of the resultant composites were characterized by scanning electron microscopy (SEM), and X-ray diffraction (XRD).

1. Introduction

Recently, semiconducting carbonates, silicates, germinates and stannates have attracted much attention, as new wide gap semiconductors. The band gap of Sr-carbonate is estimated as 3.17 eV [1]. Zinc stannate is a wide-gap semiconductor with a band gap of around 3.6 eV [2]. It has been also reported that barium stannate has a band gap of 3.4 eV [3]. One-dimensional materials have attracted much interest due to their enhanced or modified optical, electronic and mechanical properties compared to those of bulk materials.

This paper shows a preliminary growth of carbonate, stannate and silicate nano-/micro-rods. As a metallic element, sodium is chosen here due to its low melting point and high vapor pressure to make the reaction easy. The morphological and structural properties of the sodium compound nano-/micro-rods were investigated.

2. Experimental

Nano-/micro- rods were prepared with starting materials of Sn powder (99.999 %, -100 mesh), Si grain (99.999 %, 2 ~ 3 mm) and Na grain (99 %), which were weighed in an Argon gas-filled glove box and charged in boron nitride (BN) crucibles (DENKA; inside diameter, 6 mm; depth, 17 mm). The crucible was sealed in a stainless-steel tube. The sealed tube was heated in an electric

Table 1 Preparation conditions

Na - Sn

Composite	Molar ratio Na : Sn	Time (hour)	Tempreture (ºC)
#1	1.1 : 1.0	24	600
#2	1.0 : 2.0	24	600

Na – Si

Composite	Molar ratio Na : Si	Time (hour)	Tempreture (ºC)
#3	1.2 : 1.0	24	700
#4	1.2 : 1.0	24	700
#5	1.2 : 1.0	4	750
#6	1.2 : 1.0	4	650

furnace.

The details of experimental conditions are described in Table 1.

The structural properties of the resultant composites were characterized by scanning electron microscopy (SEM), Energy Dispersive X-ray Spectroscopy (EDS) and X-ray diffraction (XRD).

3. Results and Discussion

Figure 1 shows the SEM images of composite #1. From figures 1(a) and (b), a large quantity of wire-like nanostructures 0.2-1μm in diameter and 6.7-11μm in length can be observed. Moreover, it is found that several wires have needle-like shape.
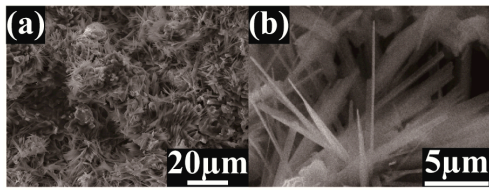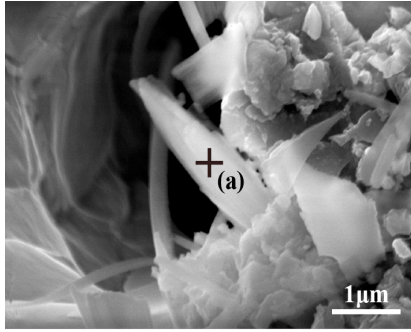
In addition, Figure 2 shows results of

Fig.1 SEM images of Composite #1 shown in Table1.

Position (at.%)	Na	Sn	O
(a)	24.59	15.90	59.44

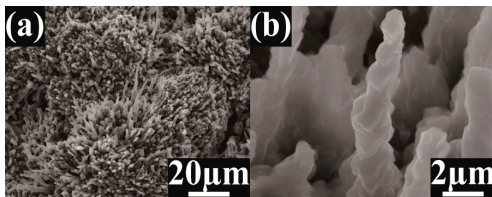Fig.2 SEM image and EDS analysis of composite #1 shown in Table1.

Fig.3 SEM images of Composite #2 shown in Table1.

SEM image and EDS analysis of composite #1. This results shows that the composition of the wires in the images of Na : Sn : O≈ 2:1:6. Therefore, this result suggests that the needle-like nano-rods consist of $Na_2(Sn(OH)_6)$.

Figure 3(a) and (b) show SEM images of composite #2. As shown in Fig.2 (a), a large number of rods were formed on the composite surface. The inukshuk-like nanostructures are formed, as shown in the Fig.2 (b). The average diameter of the rods is 1.8 μm and their lengths are in the range of about 7-10μm.

Figure 4 shows the XRD spectra of (a) composite #1 and (b) composite #2 shown in Table1. From Fig.1 (a) and (b), it is found that sodium stannate and sodium carbonate were synthesized respectively. In addition, it
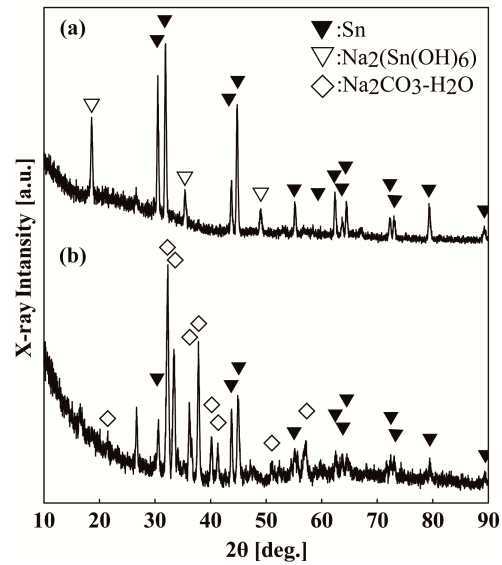

Fig.4 XRD spectra of (a) the composite #1 and (b) the composite #2.
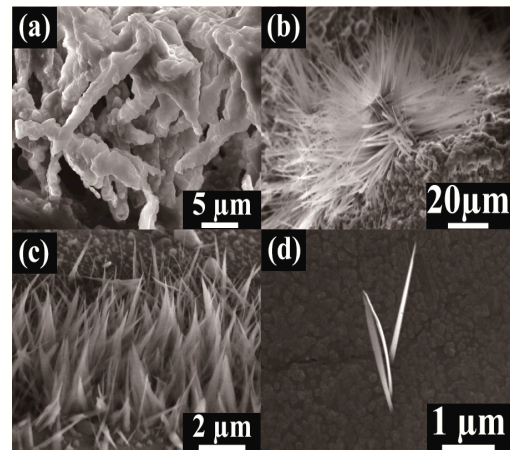

Fig.5 SEM images of (a) the Composite #5, (b) the Composite #6, (c) the Composite #7 and (d) the Composite #5.

is considered that the needle-like nano-wires synthesized with molar ratio of Na:Sn=1.1 : 1.0 consist of $Na_2(Sn(OH)_6)$ and Sn. The inukshuk-like micro-rods synthesized with molar ratio of Na : Sn=1.0 : 2.0 consist of Na_2CO_3-H_2O and Sn.

Figure 5 shows SEM images of various sodium silicate structures formed at different experimental conditions. Coral-like micro-rods and nano-wires of sodium silicate are formed at 700 ºC for 24 h, as shown in the Fig.5 (a) and (b). Moreover, the needle-like and blade-like sodium silicate nanostructures are formed at 650 ºC and 750 ºC for 4h, respectively, as shown in the Fig.5 (c) and (d).

4. Conclusion

Carbonate, stannate and silicate materials with various nano-structures were fabricated by simple experimental methods.

The molar ratio of Na : Sn affect the composition and structural property of the sodium compound. Moreover, the structural property of sodium silicate was affected by the growth temperature.

In future, new semiconducting carbonate, silicate and stannate nano-/micro-rods will be grown and their electrical and optical characterizations will be expected.

Acknowledgments

Reference

[1] S. Ni, X. Yang, T. Li, Mater. Lett. 65, 766–768 (2011).
[2] S. Baruah and J. Dutta, Sci. Technol. Adv. Mater. 12, 013004 (2011).
[3] G. Larramona, C. Gutierrez, I. Pereira, M.R. Nunes, F.M.A. Da Costa, J. Chem. Soc.Faraday Trans. 85, 907-916 (1989).

Synthesis of Ca$_2$Si Powder by Mechanical Alloying

Shingo Oda

Graduate School of Engineering, Shizuoka University
3-5-1 Johoku, Naka-ku, Hamamatsu, Shizuoka 432-8561, Japan
TEL&FAX: +81-53-478-1099
e-mail: f0130098@ipc.shizuoika.ac.jp

Abstract

Powder of Ca-silicide compounds were grown by mechanical alloying (MA). Ca-silicide compounds powder were grown in all conditions. The effect of milling energy was investigated. Some of Ca and Si powders were not reacted by MA using 5/32 inch × 16 stainless steel milling balls.

1. Introduction

Recently, semiconducting silicides have attracted much attention for their potential to create new classes of environmentally conscious electronics [1]. Because, semiconducting silicides is non- toxic and abundant materials. Alkaline-earth metal (AEM) silicides are categorized in this materials group. The growth of AEM silicides and their applications to solar cell and thermoelectric materials have been investigated [2]. AEM silicides based compounds, such as Mg$_2$Si1-xGex [3] and Mg$_2$Si$_{1-x}$Sn$_x$ [4], could be promising thermoelectric semiconductors in the middle temperature range. However, it is generally difficult to obtain highly efficient thermoelectric p-type semiconductors.

Ca$_2$Si is one of the AEM silicides, and the electronic structures of Ca$_2$Si have been calculated with the expectation of a direct transition [5, 6].

It was also reported that the orthorhombic Ca$_2$Si is a stable phase with a direct energy gap of about 0.35 eV [7]. However, its semiconducting property has not yet been experimentally determined [8]. Matsui et al. grew Ca$_2$Si layers by vapor phase growth (VPG) method using Mg$_2$Si/Si substrates [9].

Mechanical alloying (MA) is a powder processing technique that allows production of homogeneous materials starting from blended elemental powder mixtures. MA method is simple compared with VPG method. It is also possible to synthesize metastable phases with an unknown structure by MA technique [10]. It is expected that the MA method combined with the recent silicide technology would provide further development of new semiconducting silicide technologies. Warashina et al. synthesized Ca-silicide by MA. The resulting powders were contained Ca$_2$Si and/or Ca$_5$Si$_3$ phases with additional cubic phase crystals [10]. It is noted that the cubic phase of Ca$_2$Si were synthesized in the condition of the molar ratio of Ca:Si=7:3.

In this study, it was attempted that Ca-silicides were synthesized different growth condition by MA. The molar ratio of Ca:Si=7:3 was fixed. In addition, resultant powders were characterized.

2. Experiments

Ca and Si powders were synthesized by mechanical alloying. As the starting materials, fine Si powder (0.07-0.10 micrometer APS, 98%) and Ca granules (-16 mesh, 99.5%) were used. Ca and Si powders were weighed in the molar ratio of Ca:Si = 7:3. The powders and 1/8-1/4 stainless steel milling balls were placed in a steel vial under an argon atmosphere. Then, the vial was sealed by an O-ring. The milling was carried out 70 hours in a SPEX 8000 vibratory mill.

The powders structure properties were characterized by X-ray diffraction (XRD) measurements using a Cu K$_{\alpha1}$ source and scanning electron microscopy (SEM) along with energy dispersion spectroscopy (EDS).

3. Results and Discussion

Figure 1 shows X-ray diffraction patterns of the powders mechanically alloyed of Ca and Si powders under milling conditions of (a), (b) and (c), respectively defined in Fig. 1. The diffraction peaks of Ca-silicides and Si were observed for the powder synthesized under the all milling conditions. Moreover, the diffraction peak of Ca was observed for the powder synthesized under the milling condition of (b). Some of Ca and Si powders were not reacted because milling condition of (b) was the lowest energy in all conditions. However, most of Ca powders were oxidized and then CaO were changed into $Ca(OH)_2$ in the air. The diffraction peaks of Ca2Si with the cubic structure were observed under condition (b). However, PDF data of Ca_2Si with cubic structure is not determined.
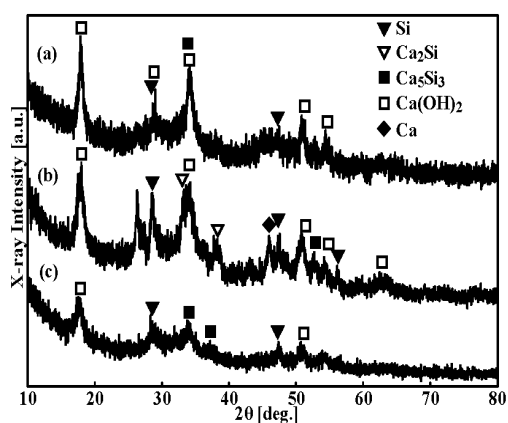
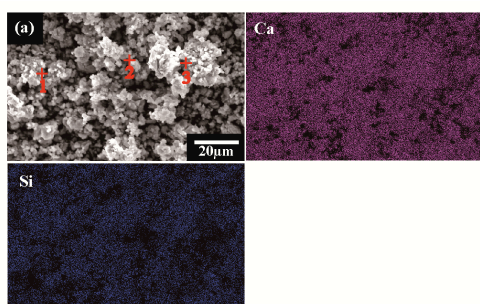Hence, the cubic structure of Ca_2Si is discussed.

Fig. 1 XRD spectra of resultant powder synthesized using the Ca granule and fine Si powder with (a) four 1/4 inch steel milling balls for 70h, (b) sixteen 1/8 inch steel milling balls for 70h, (c)sixteen 5/32 inch steel milling balls for 70h. Ca and Si powders were weighed in the molar ratio of Ca:Si = 7:3 in these cases.

Position at(%)	Ca	Si	O	Fe	Cr	Cu	Cl
001	33.84	8.96	54.13	1.51	0.59	0.50	0.48
002	33.61	8.96	54.14	1.76	0.57	0.42	0.54
003	33.42	9.15	54.23	1.78	0.49	0.54	0.39
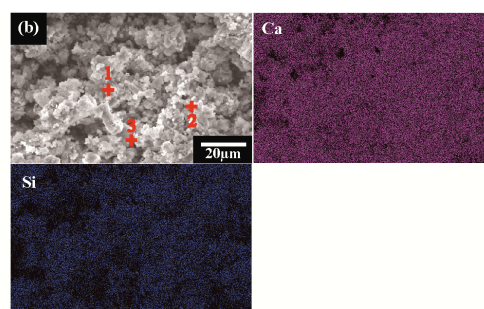
Position at(%)	Ca	Si	O	Fe	Cr	Cu	Cl
001	34.82	9.57	54.45	0.41	–	0.38	0.37
002	34.37	9.87	54.53	0.42	–	0.38	0.43
003	35.85	8.85	53.94	0.38	–	0.58	0.39
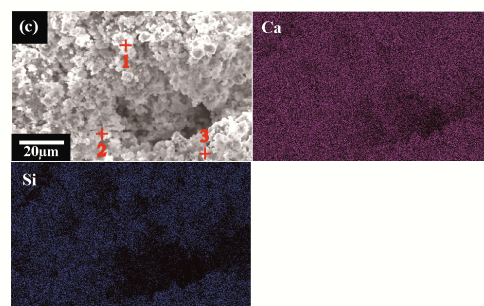
Position at(%)	Ca	Si	O	Fe	Cr	Cu	Cl
001	35.80	8.98	54.21	0.44	–	0.56	–
002	36.60	8.40	54.06	0.50	–	–	0.44
003	33.67	10.32	54.74	0.44	–	0.29	0.53

Fig. 2 SEM micrograph and the corresponding EDS analysis for the powders synthesized from Ca and Si powders with (a) four 1/4 inch steel milling balls for 70h, (b) sixteen 1/8 inch steel milling balls for 70h, (c)sixteen 5/32 inch steel milling balls for 70h. Ca and Si powders were weighed in the molar ratio of Ca:Si = 7:3 in these cases.

Figure 2 shows SEM images and the corresponding EDS analyses of the powder synthesized under the all milling conditions. The composition ratio of Ca and O were about 1:1.6 in all milling conditions. According to XRD spectra and EDS analyses, it was confirmed that Ca powders were changed into Ca-silicides and $Ca(OH)_2$. Fe and/or Cr atoms were existed in all conditions. It was considered that this result was caused by stainless milling balls. It is observed that Ca atoms were homogeneously distributed corresponding to the Si. In other words, it was considered that Ca-silicides, Si and $Ca(OH)_2$ were homogeneously distributed.

4. Conclusion

Powder of Ca-silicide compounds were grown by MA. The diffraction peaks of Ca-silicides, $Ca(OH)_2$ and Si were observed in all milling conditions. The diffraction peak of Ca was also observed for the powder synthesized under the milling condition of (b). Some of Ca and Si powders were not reacted for the powder synthesized under the milling condition of (b). Ca atoms were homogeneously distributed corresponding to the Si and the composition ratio of Ca and O were about 1:1.6 for the powder synthesized under the all milling conditions.

Reference

[1] Y. Makita, in: Mc Connel (Ed.), The First NREL Conference on Future Generation Photovoltaic Technologies, AIP, New York, 1997, p. 3.
[2] Y. Maeda, K.P. Homewood, T. Sadoh, Y. Terai, K. Yamaguchi and K. Akiyama (Eds.), Thin Solid Films, **515** (2007) 22.
[3] M. Akasaka. T. Iida, K. Nishio, Y. Takanashi, Thin Solid Films **515** (2007) 8237.
[4] J. Tani, H. Kido, J. Alloys Compd. **466** (2008) 335.
[5] Y. Imai, A. Watanabe, M. Mukaida, J. Alloys Compd. **358** (2003) 257.
[6] D. B. Migas, L. Miglio, V. L. Shaposhnikov, V. E. Borisenko, Phys. Rev. B 67 (2003) 2052031.
[7] C. Suryanarayana, Mechanical Alloying and Milling, (Marcel Dekker, New York, 1997).
[8] Y. Imamura, H. Muta, K. Kurosaki, S. Yamanaka, in: C. Uher, Y. Grin, Ballreich, Sugiwara, G. Pastorino, M. Cauchy, M. Udagawa, (Eds.), 25th International Conference on Thermoelectrics (2006) 535.
[9] H. Matsui, M. Kuramoto, T. Ono, H. Nose, H. Tatsuoka, H. Kuwabara, J. Cryst. Growth 237/239 (2002) 2121.
[10] Y. Warashina, Y. Ito, T. Nakamura, H. Tatsuoka, J. Snyder, M. Tanaka, T. Suemasu, Y. Anma, M. Shimomura, Y. Hayakawa, e-J. Surf. Sci. Nanotech. 7 (2009) 129.

Investigation on dissolution process of Si into Ge melt by X-ray Penetration Method

M.Omprakash[1,2], M.Arivanandhan[1], R. Arun Kumar [1], H.Morii[1], T.Aoki[1], T.Koyama[1], Y.Momose[1], H.Ikeda[1], H.Tatsuoka[3], Y.Okano[4], T.Ozawa[5], Y.Inatomi[6], S.Moorthy Babu[7] and Y.Hayakawa[1]

[1]Research Institute of Electronics, Shizuoka University, Hamamatsu-432 8011, Japan
[2]Graduate School of Science and Technology, Shizuoka University, Hamamatsu-432 8011, Japan
[3]Faculty of Engineering, Shizuoka University, Hamamatsu-432 8011, Japan
[4]Osaka University, Osaka, Japan
[5]Shizuoka Institute of Science and Technology, Fukuroi, Shizuoka 437-8555, Japan
[6] Japan Aerospace Exploration Agency, 3-1-1 Yoshinodai, Kanagawa 229-8510, Japan
[7]Crystal Growth Centre, Anna University, Chennai, India
E-mail-royhaya@ipc.shizuoka.ac.jp

Abstract

Si dissolution into Ge melt and crystal growth of SiGe was in-situ observed by X-ray penetration method. The rectangular shaped sandwich sample of Si (seed)/Ge /Si (feed) was used for the experiment. The penetrated X-ray intensities through the sample were recorded by rectangular shaped CdTe detector as a function of time and temperature. The experimental results demonstrate that the dissolution of Si seed was larger compared to Si feed crystal. Moreover, the crystal growth of SiGe was clearly observed from the drastic variation of penetrated X-ray intensity near the growth interface. The growth mechanism for the observed SiGe growth process was discussed based on the penetrated X-ray intensity profile and composition profile measured by EPMA.

1. Introduction

$Si_{1-x}Ge_x$ is a promising material for thermoelectric applications especially at elevated temperatures. However, it is highly challenging to optimize the figure of merit by a suitable compromise between the thermal conductivity, k, Seebeck coefficient, α, electrical conductivity, σ of the material. Moreover, the thermoelectric properties of the $Si_{1-x}Ge_x$ alloy are strongly dependent on the composition of the material [1]. Therefore to enhance the thermoelectric performance of the material, it is necessary to grow the alloy crystal with homogeneous composition. However, bulk growth of $Si_{1-x}Ge_x$ with homogeneous composition from solution is very difficult because of the large miscibility gap. Any small changes in the solidification rate lead to significant composition variations [2]. Online monitoring of the solution, composition profile and solid-liquid interface is highly useful to understand the solute transport and growth mechanism from the high temperature solution.

The enormous efforts have been made by the researcher using different methods. Nakajima et.al [3] and his group [4] developed an automated feedback control (AFC) system to keep the temperature at the interface constant during growth. Sazaki et al. observed the solution temperature distribution during the solution growth of SiGe bulk crystal using an infrared camera [5].They investigated the position of the growth interface and measured the temperature around the growth interface.

In the present study, we have investigated the dissolution of Si into Ge melt, and crystal growth of SiGe by using X-ray penetration method. The composition of the grown crystal was measured by EPMA, and discussed the dissolution process.

2. Experimental Method

Fig. 1 shows the sample configuration and the temperature profile of the furnace. Rectangular shaped Si ($6\times6\times3$ mm^3) (seed) /Ge ($6\times3\times3$ mm^3)/Si ($6\times6\times3$ mm^3) (feed) sandwich sample was used for the experiment. The samples were mirror-polished using alumina abrasive powder and etched in an acid mixture of HF: HNO_3 (1:1) (for Si) and HF:H_2O_2 (1:1) (for Ge) to remove the oxide layer. The sandwich sample filled BN crucible was inserted into the quartz ampoule and evacuated about 10^{-4} Pa before sealing. The sealed

ampoule was fixed vertically inside a furnace whose temperature profile was carefully measured before the experiment. The vertical temperature gradient at the sample position was fixed at 0.6 °C/mm. The reference temperature of the furnace was monitored using the R-type thermocouple connected at middle of the furnace.
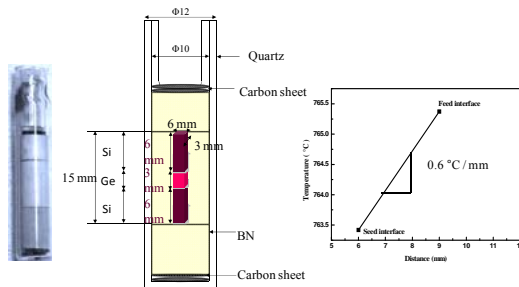

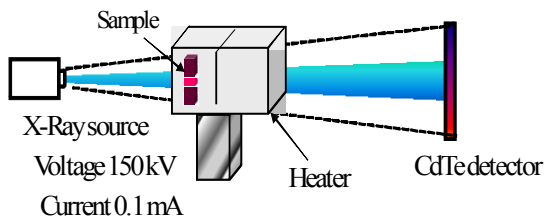Fig.1 Sample configuration and the inside temperature profile of the furnace.

Fig. 2 X-ray penetration measurement system configuration.

X-ray source is the tungsten target with an acceleration voltage of 150 kV and a current of 0.1 mA. The detector is a rectangular shaped CdTe line sensor, which has 64 cells in the x-direction and 1510 cells in the y-direction (Fig.2). The temperature of the furnace was raised up to 1200 °C at a pre-determined heating rate and maintained as constant for 5 h to observe the dissolution and crystal growth of SiGe. During heating after 660 °C, the X-rays were allowed to penetrate through the sample and the penetrated X-ray intensities were continuously recorded for every one second. Ge had completely melted when the reference temperature reached 970 °C. The composition profile of the solution was continuously observed when temperature maintained constant for 5 h. After 5 h, the temperature was

slowly decreased from 1200 °C to 1170 °C at a cooling rate of -0.42 °C/min to observe the growth from seed-solution interface.

The penetrated X-ray intensities were continuously recorded up to 800 °C during post-growth cooling. Finally, the sample was cooled down to room temperature (RT) and the penetrated X-ray intensity through the solidified sample was recorded for 1 s. The grown sample was cut parallel to the growth direction and polished with an alumina abrasive powder. The Si composition profile of the grown sample was measured along the growth direction by Electron probe micro analyzer (EPMA).
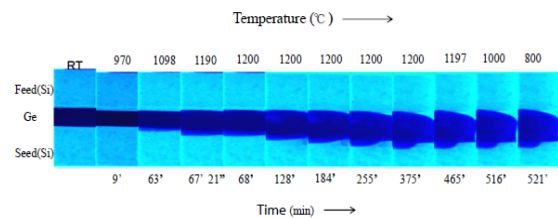
2. Results and Discussion

Fig. 3 X-ray images of the sample as a function of time and temperature.

The image at RT shows the initial dimensions of the solid Si and Ge sandwich sample. In the RT image, the Si seed and feed regions looked light blue whereas the Ge region looked dark blue due to density variation between Si and Ge. The image corresponded to Ge melting at 970 °C shows the volume change of Ge during melting. When the temperature increased, the dark blue region increased which shows the dissolution process of Si seed into Ge melt. Moreover, the darkness of the solution decreased as the time and temperature increased due to large amount of Si dissolution.

Fig. 4 illustrates the variations of the penetrated X-ray intensities during heating the sandwich sample as a function of time and temperature. The penetrated X-ray intensity of Ge was smaller than that of Si due to large density difference of Ge (5.323 g/cm^3) and Si (2.390 g/cm^3).
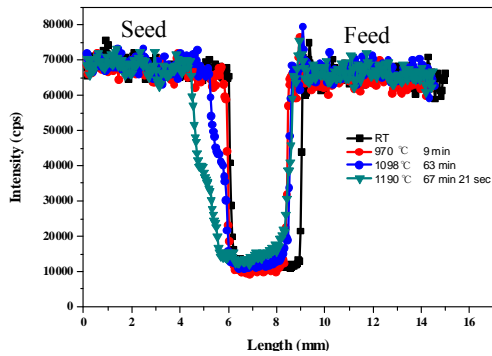
Fig. 4 Variations of penetrated X-ray intensities during dissolution with respect to time and temperature.

Fig. 5 Intensity profile at constant temperature 1200 °C with various time.

When the reference temperature reached 970 °C in 9 min, Ge was completely melted. The penetrated X-ray intensity of molten Ge was low compared with RT intensity profile and the total length of the Ge decreased from 3 to 2.7 mm due to density variation of Ge solid and liquid.

The temperature of the furnace was increased up to the desired growth temperature (1200 °C). The Si seed had started to dissolve into Ge melt as a shoulder region in the intensity profile at 1098 °C was observed in Fig. 4. The shoulder region near the seed interface and the intensity of SiGe solution region increased as the temperature increased due to continuous dissolution of Si seed into Ge melt at 1190 °C. Due to the continuous solute transport from seed interface to the feed interface, the penetrated X-ray intensity near the feed interface increased due to Si accumulation. These changes are possibly due to solute transport from seed interface by solutal convection and thus the solution near the feed interface becomes Si richer.

Once the temperature reached 1200 °C, it was kept constant for about 5 h. The intensity profile changes are shown in Fig. 5. During the dwell-time, the Si seed dissolved continuously. Moreover, the overall intensity of SiGe solution increased as the time increased and a very steep compositional gradient was established in the solution.
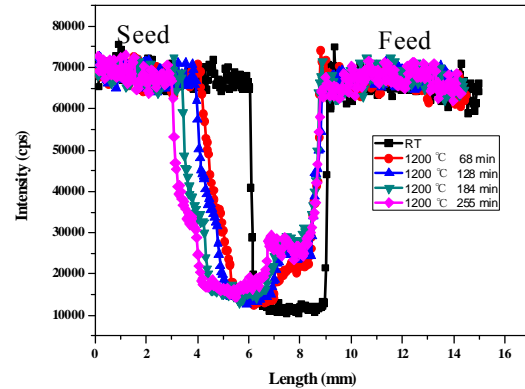
As a consequence, the solution near the feed interface got supersaturated since the inside temperature gradient between seed interface and feed interface of the sample was very low (0.6 °C/mm) as measured by dummy sample prior to the experiment (Fig. 1). Subsequently, the spontaneous growth of SiGe was started near the feed interface and it was clearly observed from the intensity profile of 128 min data. Moreover, the growth was started at the reference temperature of about 1200 °C after 128 min, thus the crystal was Si richer and the solution near the interface was Ge richer since most of the Ge was rejected from the growth interface due to segregation phenomena. The heavier Ge moved to seed interface and the dissolution of seed was proceeded further shown in Fig. 5.

Fig. 6 shows the variations of penetrated X-ray intensity profile during the cooling process of the sample. The profile at 1200 °C after 375 min shows that the dissolution stopped at the seed and feed interfaces and the growth proceeded towards seed interface. The intensity profiles at 1000 °C after 516 min and at 800 °C after 521 min indicate the overall intensity of the SiGe region increased. It shows crystallization of the residual solution during cooling process.
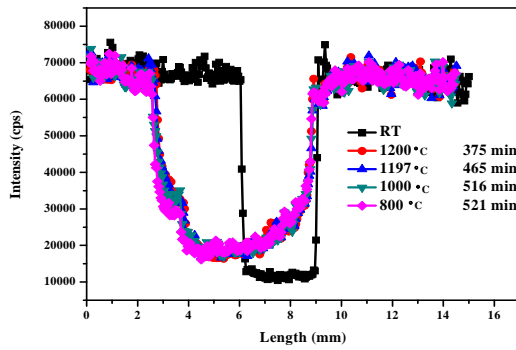
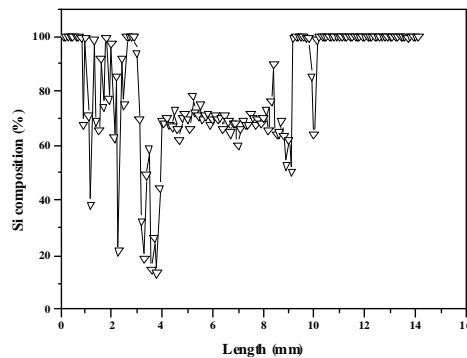Fig. 6 Intensity profile during cooling.

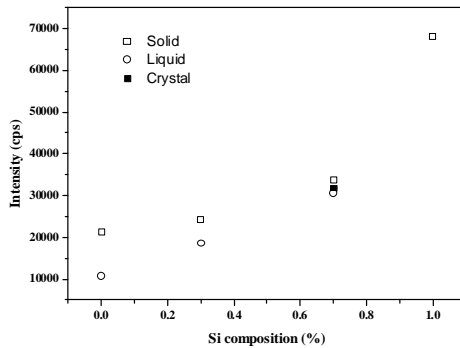Fig. 7 Si composition distribution by EPMA measurement system.

Fig. 8. Grown sample intensity compared with standard sample intensity.

After the growth process, the grown sample was removed from the ampoule and polished to study the composition distribution. Fig. 7 shows the Si compositional distribution of the grown sample by EPMA measurement. From the compositional profile it is found that the crystal was grown from the feed interface to the seed interface with the Si composition of 0.7. Near the seed interface, the composition was fluctuated and was Ge richer due to the crystallization of residual solution

during the cooling process. The composition of the grown sample was analyzed by comparing the penetrated X-ray intensity data with the standard sample and the composition of the grown sample was determined nearly $Si_{0.7}Ge_{0.3}$ as shown in Fig. 8.

4. Conclusion

Dissolution of Si into Ge melt and growth process of SiGe was in-situ observed using Si(seed)/Ge/Si(feed) sandwich sample by X-ray penetration method. The experimental results reveal that the dissolution of Si seed was dominant when compared to Si feed. The growth process was clearly observed from the time dependent X-ray intensity profile. Due to the low temperature gradient, and continuous solute transport from seed interface to feed interface, spontaneous growth had occurred near the feed interface. The composition of the grown sample was analyzed by EPMA and it well agreed with standard sample calibrated data intensity.

References

[1]   Z. Tan, W. A. Jesser and F.D. Rosi, Mat. Sci. Eng. **B 33** (1995) 195.

[2]   N.V. Abrasimov, S.N. Rossolenko, W. Thieme, A.Gerhardt, W. Schroder, J. Crystal Growth 174 (1997) 182.

[3]   K. Nakajima, S Kodama, S. Miyashita, G. Sazaki, S. Hiyamizu, J. Cryst. Growth205 (1999) 270.

[4]   Y. Azuma, N. Usami, T. Ujihara, G. Sazaki, Y. Murakami, S. Miyashita, K.Fujiwara, K. Nakajima, J. Cryst. Growth 224 (2001) 204.

[5]   N. Armour and S. Dost, J. Crystal Growth **311**(2009)780.

PbSrS based quantum well for optically pumped surface emitting laser

Yutaro Sugiyama

Department of Electrical and Electronic Engineering, Shizuoka University,
Johoku 3-5-1, Naka-ku Hamamatsu 432-8561, Japan

Abstract

This paper introduces theoretical background and design of quantum well for optically pumped mid-infrared surface emitting laser. To obtain high optical gain we use multiple quantum well (MQW) structure. We calculated the theoretical value of quantum well's gain.

1. Introduction

Tunable mid-infrared lasers are useful for spectroscopic applications such as trace gas analysis, high speed gas detection. A high non-radiative Auger-recombination probability and a large free carrier absorption which is proportional to the wavelength squared are making difficult to prepare mid-infrared semiconductor lasers operating at room temperature. Lead salt IV-VI materials such as PbTe, PbSe, and PbS have direct gaps at L-points of Brillouine zone and have almost symmetric band structure between conduction and valence bands. Thus the Auger recombination probability is much smaller than that of III-V and II-VI materials, and relatively higher temperature laser operation have been obtained in the IV-VI materials [1,2]. Optically pumped lasers are useful to decrease the optical losses by free carrier absorption [3]. We recently prepared SrS/PbS multiple quantum well (MQW) VECSELs with optically excitation (OE) layers in both sides of the active layers [4,5]. The MQW laser operated in high efficiency and high power at -70°C with external quantum efficiency of 16% and maximum pulsed output power of 2W. We describe here a theory and design of quantum well for optically pumped PbS-based active layer.

2. Density of States(DOS)

Density of states for bulk material is given by

$$D_{3D}(E) = 2\frac{d}{dE}\left(\frac{\frac{4}{3}\pi k^3}{(2\pi)^3}\right) . \tag{1}$$

E-**k** relationship at the bottom of conduction band or the top of valence band is given by

$$E = \frac{\hbar^2 k^2}{2m} , \tag{2}$$

where $\hbar$ is plank constant and m is effective mass. Therefore, density of states for bulk material is given by

$$D_{3D}(E) = \frac{\sqrt{2m^3 E}}{\pi^2 \hbar^3} . \tag{3}$$

Also two-dimensional density of states for quantum well is given by

$$D_{2D}(E) = \frac{m}{\pi \hbar^2}\sum \Theta(E - E_n) , \tag{4}$$

where E_n is the band edge energy of the n-th subband, and $\Theta(E-E_n)=1$ for $E-E_n \geq 0$ and $\Theta(E-E_n)=0$ for $E-E_n < 0$.
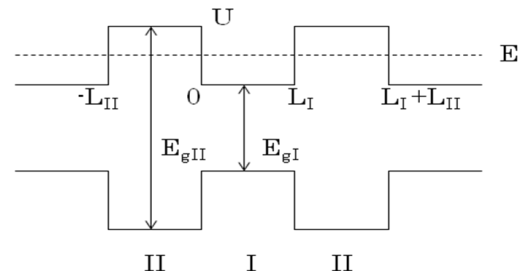
IV-VI materials has the property that

Fig.1 Schematic band diagram of a superlattice.

shapes of constant energy surfaces is ellipsoids of revolution along the <111> axes. Therefore, electron and hole have two kinds of effective masses; m_l and along the symmetry axes and m_t transverse to the symmetry axes. So the E-$\mathbf{k}$ relationship becomes as follows.

]

$$E\left(1+\frac{E}{E_g}\right) = \frac{\hbar^2}{2}\left(\frac{k_x^2}{m_t}+\frac{k_y^2}{m_t}+\frac{k_z^2}{m_l}\right) \qquad , (5)$$

where E_g is the band gap and the term $(1+E/E_g)$ represents nonparabolicity near the band edge, based on two-band model. Thus, three dimensional density of states is given by

$$D_{3D}(E) = \frac{\sqrt{2m_t^2 m_l E}}{\pi^2\hbar^3}\sqrt{1+\frac{E}{E_g}}\left(1+\frac{2E}{E_g}\right) , \qquad (6)$$

and two-dimensional density of states is given by

$$D_{2D}(E) = \frac{\sqrt{m_t^2 m_l/m_{zz}}}{\pi\hbar^2}\left(1+\frac{2E}{E_g}\right)\sum\Theta(E-E_n) \quad (7)$$

where m_{zz} is the effective mass along quantum well direction given by

$$1/m_{zz} = \left(\cos^2\theta/m_l\right)+\left(\sin^2\theta/m_t\right). (8)$$

As usual, boundary conditions of the wave function at the materials boundary I / II are

$$\Phi_I = \Phi_{II}$$

$$-\frac{d\Phi_I/dz}{E+E_{gI}} = \frac{d\Phi_{II}/dz}{E+E_{gII}-U}$$

(9)

and

(10)

In superlattice shown in Fig.1, the Bloch condition $\Phi(z+L) = \Phi(z)\exp(ikL)$ must be fulfilled, resulting in the following equation for the subband structure of the superlattice with layer thicknesses L_I and L_{II}:

$$-\frac{\xi+1/\xi}{2}\sin(k_{zI}L_I)\sin(k_{zII}L_{II})$$
$$+\cos(k_{zI}L_I)\cos(k_{zII}L_{II}) = \cos(k(L_I+L_{II})) \qquad (11)$$

, where

$$\xi = k_{zI}\left(E+E_{gII}-U\right)/k_{zII}\left(E+E_{gI}\right) . \qquad (12)$$

By solving the above equation, the E-$\mathbf{k}$ relationship of superlattice consisting of several subbands and density of states are obtained as shown in Fig.2. The density of states for each subband is represented by a two-dimensional density of states.

In PbS, there is one valley along [111] superlattice direction and 3 oblique valleys along other <111>.

3. SrS/PbS SPSL and optical gain

We used SrS/PbS short-period superlattices (SPSLs) with atomic layer SrS for the barrier layers in the MQWs. The SPSL has higher carrier mobility compared to PbSrS alloy owing to smaller alloy
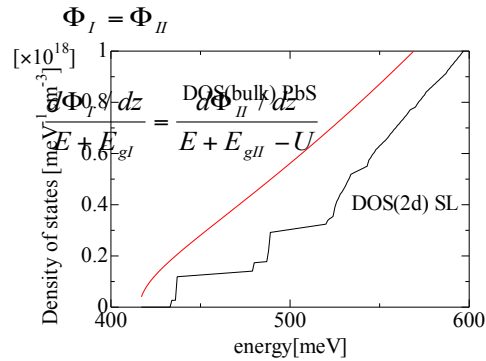
Fig.2 Density of states for PbSrS/PbS (111) MQW with 12nm PbSrS barrier and 8nm PbS well. Small and large steps in the density of states correspond to [111] and other <111> oblique valleys.
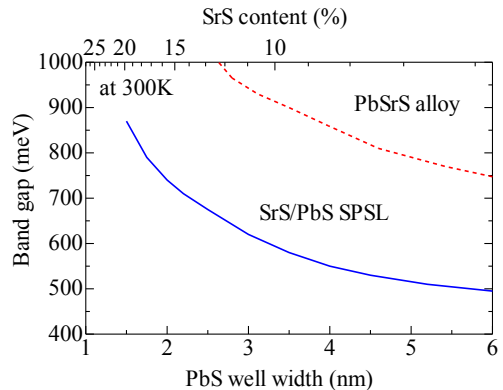

Fig.3 Band gaps of SrS/PbS SPSL with monolayer SrS and PbSrS alloy with the same SrS content.

scattering. And the higher mobility is useful to decrease free carrier absorption because free carrier absorption is inversely proportional to the mobility [4,5]. Figure3 shows the band gap of the PbSrS SPSL, and that of PbSrS alloy with same SrS content. The band gap of the SPSL increases with the decrease of the PbS layer thickness.

Absorption coefficient is proportional to density of states. The absorption coefficient is obtained simulating of the theoretical
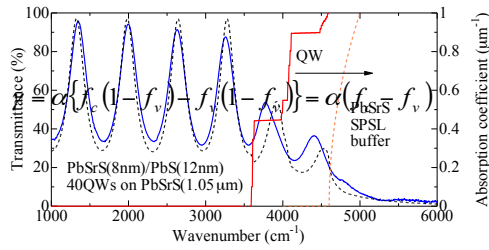

Fig.4 Optical transmission spectra of PbSrS/PbS 40MQW, grown on PbSrS buffer layer. BaF$_2$(111) was used for the substrate. PbSrS layer consists of SrS/PbS(12nm) SPSL. Black dashed line shows theoretical transmission spectrum calculated from the indicated absorption coefficients (solid line in red color), and blue line shows experimental spectrum.
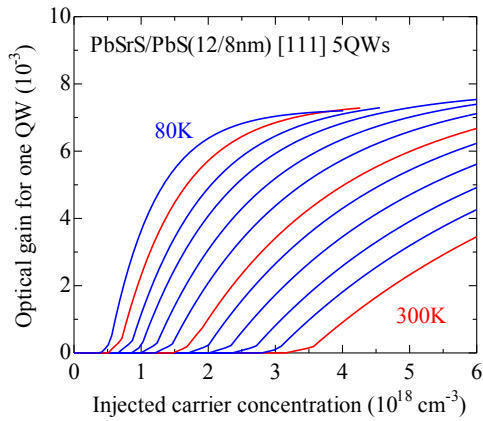

Fig.5 Dependence of optical gain on injected carrier concentrations for PbSrS/PbS MQW from 80 to 300K.

transmission spectrum to the experimental one.

The optical gain γ is obtained by following equation.

$$\tag{13}$$

Fig.5 shows the dependence of optical gain for one PbS quantum well grown in [111] direction on excitation carrier density with the parameter of temperature from 80K to 300K. Maximum gain per one quantum well is about 0.002 at 300K with excited carrier concentration $n=p=5\times10^{18}$cm^{-3}. Thus, if we prepare the active layer with 5QWs, mirror reflectivity above 99% is necessary to obtain laser operation.

4. Summary

Theoretical background and design of quantum wells for optically pumped mid-infrared surface emitting lasers were described. To obtain enough optical gain   a multiple quantum well (MQW) structure is necessary. With the mirror reflectivity about 99%, number of quantum wells around five is necessary for room temperature laser operation.

Reference

[1] D. L. Partin, Superlattices and Micro-structures **1**, 131 (1985).

[2] B. Spanger, U. Schiessl, A. Lambrecht, H. Böttner, and M. Tacke, Appl. Phys. Lett. **53**, 2852 (1988).

[3] A. Khiar, M. Rahim, M. Fill, F. Felder, F. Hobrecker, and H. Zogg, Appl. Phys. Lett. **97**, 151104 (2010)

[4] A. Khiar, M. Rahim, M. Fill, F. Felder, H. Zogg, D. Cao, S. Kobayashi, T. Yokoyama, and A. Ishida, J. Appl. Phys. **110**, 023101 (2011)

[5] A. Ishida, Y. Sugiyama, Y. Takano, H. Sakata, M. Rahim, A. Khiar, M. Fill, F. Felder, and H. Zogg, submitted to Appl. Phys. Lett. **99**, 121109 (2011)

The effect of Ca substitution for Ba on the superconductor $YBa_2Cu_3O_y$

Toru Tanikawa[*] and Yasuhiro Hayakawa

Research Institute of Electronics, Shizuoka University,
3-5-1 Johoku, Naka-ku, Hamamatsu, Shizuoka 432-8011, Japan
TEL&FAX: +81-53-478-1338
[*]e-mail: rt2senor@hotmail.co.jp

Abstract

Characteristic changes by the substitution of Ca for Ba in $YBa_2Cu_3O_y$ superconductors have been investigated. The pellets were characterized by scanning electron microscope (SEM) together with X-ray energy dispersive spectroscopy (EDS), X-ray diffraction (XRD) and magnetic susceptibility measurement. It was found that the sample didn't show superconductivity between 56 K and room temperature. CaO rich precipitates were formed.

1. Introduction

The high-temperature superconductivity at 30 K in the oxide compound $(LaBa)_2CuO_4$ was discovered by Bednorz and Muller [1] in 1986. Soon after that Cho et al. and Wu et al. [2-3] found the superconducting transition temperature around 90 K in Y-Ba-Cu oxide system. These discovery of high-T_c superconductors simulated many researchers to investigate new oxide superconductors with higher T_c and extensive studies have been made on various properties of these oxides. Up to now, however, the highest T_c is 164 K which is recorded on $Hg_2Ba_2Ca_2Cu_3O_w$ at high pressure [4].

In order to find high-T_c superconductors, we have investigated about the effect of substitution of Ca for Ba on the $YBa_2Cu_3O_y$ superconductor.

2. Experimental

At first, the standard $YBa_2Cu_3O_x$ superconductor was synthesized for a reference. Y_2O_3, $BaCO_3$ and CuO of reagent-grade purity were used as source materials. It was sintered at 900 °C for 12 h in air and then it was reground and cold-pressed into disk-shape pellets. The pellets were sintered at 960 °C for 12 h in air, after that the furnace was cooled to 500 °C and annealed in O_2 atmosphere at 24 h, then, finally the furnace was cooled to room temperature at a slow speed.

Three kinds of samples (samples A, B, C) were synthesized from powders of Y_2O_3, $CaCO_3$ and CuO of reagent-grade purity. For the synthesis of all samples, the appropriate amounts of powers were mixed. Figs. 1(a) and (b) show the pre-sintering, sintering and annealing processes of the sample A, respectively. It was sintered at 960 °C for 12 h in air, thoroughly reground and cold-pressed into disk-shape pellets. The pellets were sintered at 960 °C for 12 h in air, after that the furnace was cooled to 500 °C and annealed in O_2 atmosphere at 24 h, then, finally the furnace was cooled to room temperature at a slow speed.

Sample B was sintered under O_2 atmosphere in all the above processes. The temperature and time conditions of sample B was the same as the conditions of sample A. For the sample C, the temperature-condition was changed during the first sintering process. The temperature was decreased to 1000 °C for the sintering process of samples C. The atmosphere and time conditions of sample C was the same as the conditions of sample A.

The surface morphological, compositional and structural properties of all the samples were analyzed using Scanning Electron Microscopy (SEM), Energy Dispersive Spectroscopy (EDS) and X-ray powder diffraction (XRD) apparatus. Magnetic susceptibility measurements were performed by an AC susceptibility- temperature measurement, using a CHINO SK03-01A.
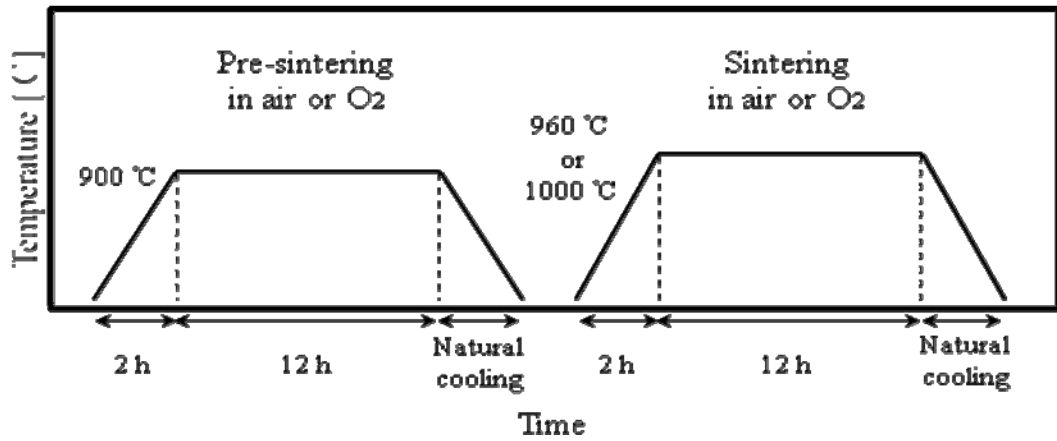
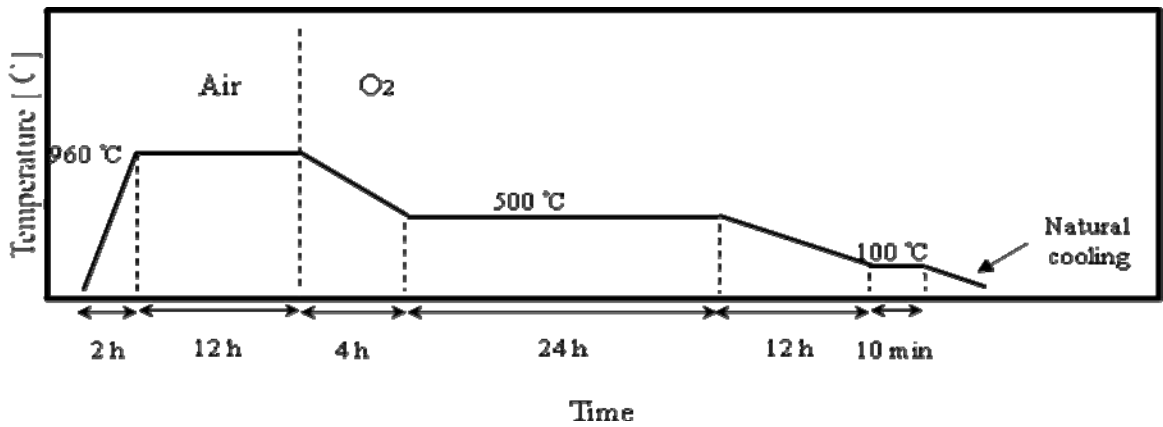Fig. 1(a)   Pre-sintering and sintering processes.

Fig. 1(b)   Annealing process.

3. Results and Discussion

3-1 YBa$_2$Cu$_3$O$_x$ superconductor

Fig. 2 shows XRD pattern of the standard YBa$_2$Cu$_3$O$_x$ superconductor. It indicated an orthorhombic structure and the lattice constant was a = 3.7845, b = 3.9225 and c = 11.6367 Å

The temperature dependence of the magnetic susceptibility is shown in Fig. 3. The critical temperatures which are 10 % and 90 % of the change of susceptibility from the normal state were 89.4 and 90.2 K, respectively.

Fig. 2   XRD pattern of the standard YBa$_2$Cu$_3$O$_x$ perconductor.

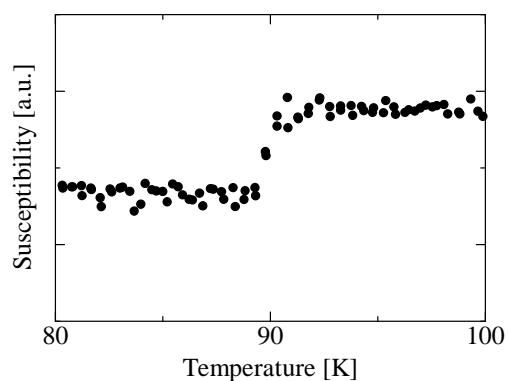## 3-2 Substitution of Ca for Ba on the YBa$_2$Cu$_3$O$_y$

The XRD pattern of sample A is shown
in Fig. 4. The pattern was different from the
YBa$_2$Cu$_3$O$_y$ (Fig. 2). It suggested that the
crystal structure of sample A was not same
as the YBa$_2$Cu$_3$O$_y$ structure and Ca was not
simply substituted of the Ba site. The sam-
ples B and C also indicated the same struc-
tures.

Figure 5 shows the surface morphology
of sample A recorded by SEM. The compo-
sition of the P and Q area were measured by
EDS. The ratio of Y : Ca : Cu : O was 13.3 :
16.7 : 34.3 : 35.7 at the area P and 1.2 :
51.8 : 3.7 : 43.3 at the area Q. It indicated
that CaO-rich precipitates were formed at the
area Q. To make clear the distribution of the
elements, the mapping of the Y, Ca. Cu and
O was measured as shown in Fig. 6. It was
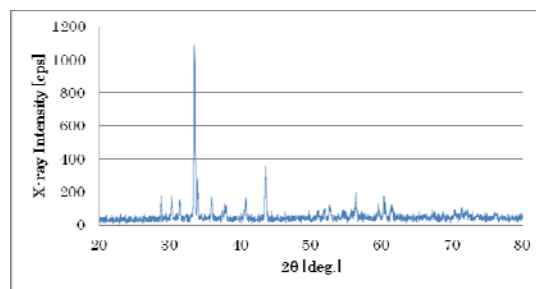clearly seen that the Ca rich area were in-
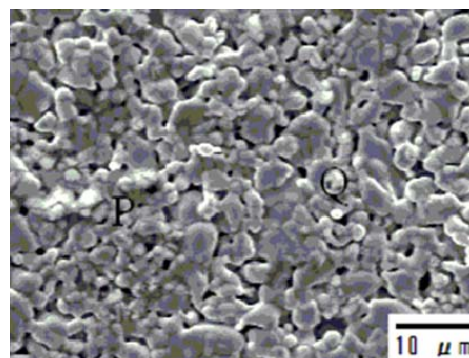cluded in the sample.

Fig. 4   XRD pattern of the sample A.

Fig. 5 Surface morphology of sample A
asured by SEM.

The temperature dependence of the
magnetic susceptibility is shown in Fig. 7.
The sample A did not indicate the supercon-
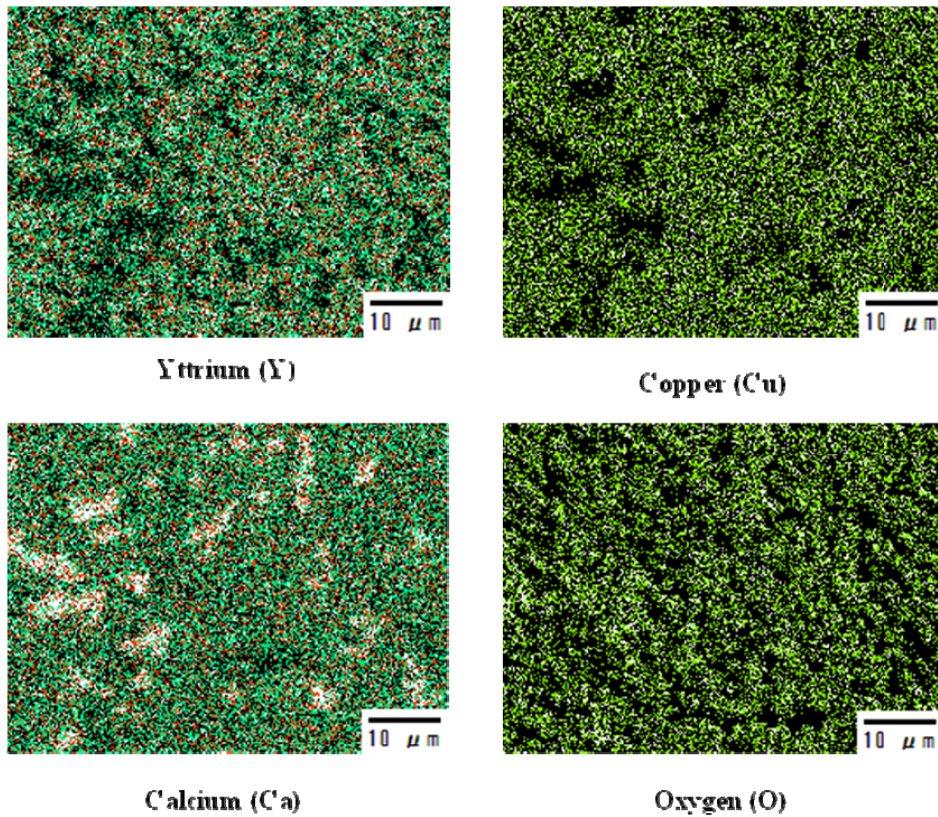ductivity between 56 K and room tempera-
ture

Yttrium (Y)

Copper (Cu)

Calcium (Ca)

Oxygen (O)

Fig. 6 the mapping of the Y, Ca. Cu and O.
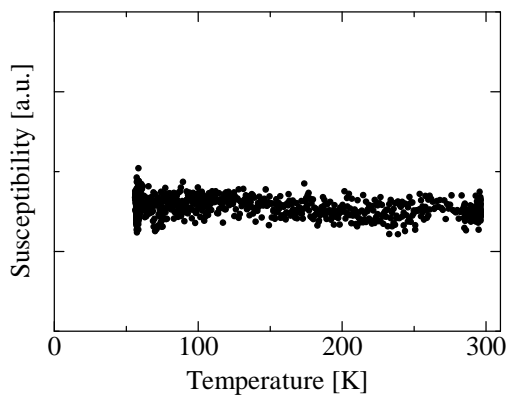

Fig. 7   The temperature dependence of the
agnetic susceptibility of the sample A.

4.   Conclusion

YBa$_2$Cu$_3$O$_x$ standard sample was synthe-
sized and measured the superconducting
properties. Samples which substitute Ca for
Ba on the YBa$_2$Cu$_3$O$_y$ did not show super-
conductivity between 56 K and room tem-
perature. The crystal structure was different
from YBa$_2$Cu$_3$O$_y$. CaO rich precipitates were
formed.

Reference
[1] J.G.Bednorz, K.A.Mueller, Z.Phys.B64
(1986) 189.
[2] C.W.Chu, P.H.Hor, R.L.Meng, L.Gao,
Z.J.Haung, Y.Q.Wang, J.Bechold,
D.Cambel, M.K.Wu, J.Ashburn and
C.H.Haung Phy.Rev.Lett.58 (1987) 405.
[3] M.K.Wu, J.R.Ashburn, C.J.Torng,
P.H.Hor, R.L.Meng, L.Cao, Z.L.Hung,
Q.Wang and C.W.Cho, Phys. Rev. Lett.
58 (1987) 908.
[4] A.Schilling, M.Cantoni, D.J.Guo and
H.R.Ott, Nature 363 (1993) 56.